

1 **Observed multiscale dynamical processes responsible for an**
2 **extreme gust event in Beijing**

3
4 Xiaoran Guo^{a,b}, Jianping Guo^a, Ning Li^a, Zhen Zhang^{a,c}, Tianmeng Chen^a, Yu
5 Shi^d, Pengzhan Yao^{a,c}, Shuiru Jiang^a, Lei Zhao^b, Fei Hu^d

6
7 ^aState Key Laboratory of Severe Weather Meteorological Science and Technology &
8 Specialized Meteorological Support Technology Research Center, Chinese Academy of
9 Meteorological Sciences, Beijing 100081, China

10 ^bKey Laboratory of South China Sea Meteorological Disaster Prevention and Mitigation of
11 Hainan Province, Haikou 570203, China

12 ^cDepartment of Atmospheric and Oceanic Sciences and Institute of Atmospheric Sciences,
13 Fudan University, Shanghai 200438, China

14 ^dState Key Laboratory of Atmospheric Environment and Extreme Meteorology, Institute of
15 Atmospheric Physics, Chinese Academy of Sciences, Beijing 100029, China

16
17
18
19
20
21
22 Correspondence to:

23
24 Dr./Prof. Jianping Guo (Email: jpguocams@gmail.com)

Formatted: Font: Times New Roman

Formatted: Font: Times New Roman

Abstract

Extreme wind gusts pose substantial threats to human safety and infrastructure, yet inadequate pre-onset observational constraints result in large uncertainties and inaccuracies in nowcasting and forecast. To address this gap, we conduct an in-depth investigation of a record-breaking surface gust event (wind speed $>35 \text{ m s}^{-1}$) that occurred in Beijing during the early afternoon of 30 May 2024. We analyze the event's dynamical characteristics utilizing a high-resolution meteorological mesonet, which includes seven radar wind profilers (RWPs), a meteorological tower, automated weather stations, radar and satellite data. Multi-source observational analyses reveal that multicellular storm developed ahead of a convergence line, where northeasterly cold outflows collided with environmental southerly winds during their downhill propagation. Evaporative cooling drove the generation of extreme winds, reinforced by downward momentum transport and pressure gradient forcing. After reaching the plain, two convective segments subsequently merged into a well-organized squall system embedded with a midlevel mesovortex with intense rear-inflow jet. Low-level frontogenesis and shearing deformation provided favorable conditions for sustaining mesoscale convection, which in turn fueled small-scale turbulent energy processes. Turbulent inverse energy cascades—energy transfer from small to large eddies—intensified markedly as wind speeds increased. This study offers valuable insights into the multiscale dynamical processes governing convective evolution—captured by the RWP mesonet—that would otherwise remain inaccessible via other ways. Importantly, these findings support the validation of numerical simulation outputs, refinement of boundary-layer parameterization schemes in numerical weather prediction (NWP) models, and ultimately the enhancement of forecast skill for convection-associated extreme gust events.

Key words: Extreme winds, Radar wind profilers, Quasi-linear convective systems, Turbulence

Deleted: remain inadequate, leading to

Deleted: prediction

Deleted: explore

Deleted: of this event

Deleted: show

Deleted: the development of

Deleted: the

Deleted: as the

Deleted: met

Deleted: its

Deleted: contributed to

Deleted: the

Deleted: through the

Deleted: The emergence of

Deleted: 1

Deleted: . This mesoscale convection then

Deleted:

Deleted: he

Deleted: of turbulence

Deleted: a process involving

Deleted:

Deleted: significantly

Deleted: markedly

Deleted: This study provides valuable insights into capturing the multiscale dynamical processes governing convective evolution by high-resolution vertical observations, especially the RWP mesonet. It's helpful to validate the numerical simulation results of other studies and improve assimilation schemes and parameterizations in weather forecasting ... [1]

Formatted ... [2]

Deleted: alternative

Deleted: observational or analytical approaches

Deleted: these findings are of significant value for validation ... [3]

Deleted: This study offers valuable insights into the ... [4]

Formatted: Font: Times New Roman

108

109

Short Summary

110

111 Wind gusts threaten safety and infrastructure but are hard to predict. To address this
112 gap, we studied an extreme wind gust event in Beijing on May 30, 2024. We used seven
113 radar wind profilers to track how this gust developed. It formed when cold northeasterly
114 air clashed with warm southerly winds as the storm moved downhill. Evaporation of
115 rain cooled the air, boosting downward air movement and wind strength. The
116 turbulence transferring energy from small to large eddies intensify winds.

117

1. Introduction

Extreme intense winds rank among the most destructive meteorological hazards globally, causing cascading disasters such as infrastructure collapse, wildfire escalation, and aviation accidents (Goyette, 2003; Pryor and Barthelmie, 2010; 2011; Peterson et al., 2014). However, large uncertainties in the wind speed estimations still exist in weather forecast models and reanalysis products (Azorin-Molina et al., 2016; Torralba et al., 2017; Kahl, 2020; Hirt and Craig, 2021; Pryor and Barthelmie, 2012; 2021; Wu et al., 2024), especially for those associated with convection-induced extreme wind gusts, due partly to limitations in spatial resolution and parameterization schemes (Fovell, 2002; Fiori et al., 2011; Adams-Selin et al., 2013; Burghardt et al., 2014).

Wind gusts—short-lived extreme events—arise when air with high momentum is transported to the surface (Harris and Kahl, 2017). They occur alongside both convective and non-convective processes and are affected by a range of physical factors, including wind speed, turbulence in the planetary boundary layer (PBL), topographic flows, and surface roughness (Letson et al., 2018). In previous convection-induced wind gust research, the role of a complex interplay of factors has been well recognized. Specifically, mesoscale dynamics and thermodynamics interaction drives the generation of downdrafts to form the initial “engine” of the gust (Johns and Hirt 1987; Vose et al., 2014; Abulikemu et al., 2019; Taszarek et al., 2019). Microphysics processes governs latent cooling rates, which directly control the buoyancy and strength of downdraft (Mahoney and Lackmann 2011; Adams-Selin et al. 2013; Zhou et al. 2020). Then, the turbulence-convection interaction modulates these downdrafts and outflows by turbulent mixing near the surface and determines how efficiently momentum is transferred to the surface, thereby sharpening or dissipating the gust front (Tucker et al., 2009; Tang et al., 2015; Shao et al., 2023a; 2023b).

Among others, quasi-linear convective systems (QLCSs) such as squall lines can produce a straight-line swath of extreme winds (Fujita 1978; Johns and Hirt 1987;

Deleted: Page Break

Deleted: Pryor and Barthelmie, 2010; 2011

Deleted: &

Deleted: Kahl, 2020;

Deleted: Torralba et al., 2017;

Deleted: Fiori et al., 2011; Fovell, 2002

Deleted: &

Deleted: , such as

Deleted:

Deleted: Johns & Hirt 1987;

Deleted: Vose et al., 2014

Deleted: ,

Formatted: Font: Times New Roman

Formatted: Font: Times New Roman

Deleted: ini

Deleted: turbulence-convection interaction

Deleted: (Shao et al., 2023a; 2023b; Tang et al., 2015; Tucker et al., 2009), and microphysics processes and dynamics interactions (Adams-Selin et al. 2013; Mahoney and Lackmann 2011; Zhou et al. 2020).

164 Coniglio et al., 2011; Meng et al. 2012; Xu et al., 2024). Given their damaging potential,
 165 many efforts have been made in the past few decades to explore the mechanisms of
 166 extreme wind gusts generated by QLCSs in observational and numerical studies (e.g.,
 167 Lafore and Moncrieff 1989; Bentley and Mote, 1998; Atkins et al., 2005; Meng et al.
 168 2012). It was consistently found that the intensity of cold outflows is one of the main
 169 contributors of extreme wind gusts (Houze, 2014; Haerter et al., 2019; Chen et al.,
 170 2024). The formation of mesoscale vortices (Wheatley and Trapp 2008; Atkins and
 171 Laurent, 2009; Evans et al., 2014; Xu et al., 2015b; Zhang et al., 2021) and the merger
 172 of convective cells (French and Parker; 2012; 2014; Liu et al., 2023; Yang and Du,
 173 2026) have a close connection with the evolution of QLCSs and the initiation of
 174 extreme wind gusts. The midlevel rear-inflow jet (RIJ) in the stratiform region of
 175 QLCSs plays an important role in strengthening the extreme winds at the surface via
 176 the downward transport of momentum (Zhang and Gao 1989; Weisman, 1992; Grim et
 177 al., 2009; Browning et al., 2010; Xu et al., 2015a).

Deleted: Fujita 1978; Johns & Hirt 1987;

Deleted: Bentley & Mote, 1998;

Deleted: ; Lafore and Moncrieff 1989

Deleted: ; Haerter et al., 2019; Houze, 2014

Deleted: &

Deleted: Wheatley & Trapp 2008;

Deleted: Grim et al., 2009; Weisman, 1992;

Deleted: ; Zhang & Gao 1989

Deleted: some

178 Although the above-mentioned studies have made significant progress in
 179 quantifying the characteristics of QLCSs, reliable QLCS-induced gust forecasting
 180 remains challenging to achieve. This is mainly because the energy-carrying turbulent
 181 eddies that harbor gusts are typically far too small to be resolved by observational
 182 networks and mesoscale numerical models (Fovell and Cao, 2014). To the best of our
 183 knowledge, most of previous studies, nevertheless, relied on the model simulation or
 184 reanalyses. This leads to large knowledge gaps in the vertical structure of lower
 185 troposphere and its evolution in the presence of QLCS, especially for highly localized
 186 and transient storms (Luchetti et al., 2020; Romanic et al., 2020).

Deleted: As such, more studies are urgently needed to elucidate the multiple scales of interaction for an in-depth understanding of the formation mechanisms that create extreme wind gust events.

187 To confront this challenge, high-resolution vertical wind observations from wind
 188 towers have been widely applied to elucidate the atmospheric dynamic structure and
 189 evolving convective morphology leading to damaging winds (e.g., Bélair et al., 2025).
 190 Nevertheless, the wind tower cannot capture the winds near clouds, resulting in large
 191 vertical wind observations gaps especially, which can be overcome by the radar wind

Deleted: In this regard,

Deleted: detailed

Deleted: are essential for capturing the

208 profiler (RWP, Liu et al., 2024). A high-density RWP network has been setup in China
 209 (Guo et al., 2021a) since 2008a, especially in Beijing and the Yangtze River Delta
 210 (YRD). The continuous vertical measurements from RWP, along with meteorological
 211 towers, afford us a valuable perspective to shed light on these complex phenomena. For
 212 instance, Chen et al. (2024) examined a record-breaking surface gust wind that
 213 occurred in eastern China on 30 April 2021 by using the measurements from the RWP,
 214 mesonet in the YRD region.

215 Here we examine an extreme wind gust event associated with a QLCS that
 216 occurred in Beijing on 30 May 2024, where the climate and terrain are quite different
 217 from YRD. The instantaneous surface wind speeds at 250 sites in this event exceeded
 218 17.2 m s^{-1} with the maximum wind speed reaching 37.2 m s^{-1} . This high-wind-
 219 producing convective system caused widespread fallen trees and power lines, damaging
 220 many vehicles and buildings. This intense wind gust event is comprehensively analyzed
 221 by using a high-resolution meteorological mesonet consisting of seven RWPs and one
 222 meteorological tower in an attempt to gain insight into the vertical structural evolution
 223 within the PBL and elucidate the complex multi-scale dynamical processes during the
 224 event. The next section describes the data and methodology used in this work. Section
 225 3 presents an overview of the QLCS and associated extreme wind gust event. In Section
 226 4, the utility of the RWPs and meteorological tower mesonet in capturing the evolving
 227 vertical structure of the high-wind event is examined. Key findings are concluded in
 228 the final section.

229 2. Data and Methodology

230 2.1 Vertical profile measurements

231 Figure 1a presents the spatial distribution of RWP mesonet deployed in Beijing,
 232 which is composed of seven stations. These RWPs are Ce Feng Leida-6 (CFL-6)
 233 Tropospheric Wind Profilers, which are produced by the 23rd Institute of China
 234 Aerospace Science and Industry Corporation (Liu et al., 2020). They provide

Deleted: As of 2010's, a

Deleted: High-density

Deleted: of wind profiles provided by ground-based mesonet observations, including radar wind profiler (

Deleted:)

Deleted: and

Deleted: Chen et al. (2024) examined a record-breaking surface gust wind event that occurred in eastern China on 30 April 2021 by using data from a network of radar wind profilers in the Yangtze River Delta (YRD) region.

Deleted: ¶

Formatted: Font: Not Bold, Not Italic, Complex Script Font: Not Bold, Not Italic

Formatted: Font: Times New Roman, 12 pt, Not Bold, Not Italic, Complex Script Font: 12 pt, Not Bold, Not Italic

Formatted: Font: Not Bold, Not Italic, Complex Script Font: Not Bold, Not Italic

Formatted: Font: Times New Roman, 12 pt, Not Bold, Not Italic, Complex Script Font: 12 pt, Not Bold, Not Italic

Formatted: Font: Times New Roman, 12 pt, Not Bold, Not Italic, Complex Script Font: 12 pt, Not Bold, Not Italic

Deleted: Yangtze River Delta (YRD)

Deleted: of China

Formatted: Font: Not Bold, Not Italic, Complex Script Font: Not Bold, Not Italic

Deleted: As such, more studies are urgently needed to elucidate the multiple scales of interaction for an in-depth understanding of the formation mechanisms that create extreme wind gust events. ¶

Deleted: .

Deleted: Here, t

Deleted: the following six

Deleted: : Haidian (HD; 39.98°N, 116.28°E), Huairou (HR; 40.36°N, 116.63°E), Yanqing (YQ; 40.45°N, 115.97°E), Shangdianzi (SDZ; 40.66°N, 117.11°E), Pinggu (PG; 40.17°N, 117.12°E), Xiayunling (XYL; 39.73°N, 115.74°E), and the Beijing Weather Observatory (BWO; 39.79°N, 116.47°E)

Deleted: ¶

262 measurements of horizontal and vertical winds, and refractive index structure parameter
263 at 6-min intervals. The vertical resolution is 120 m from 0.15 to 4.11 km above the
264 ground level (AGL) in low-operating mode, and 240 m from 4.11 to 10.11 km AGL in
265 high-operating mode. After testing the data quality of the RWPs in our previous study
266 (Guo et al., 2023), horizontal wind speed, direction and vertical velocity derived from
267 RWPs in the heights of 0.51–4.95 km AGL were found to be reliable. Linear
268 interpolation in time is adopted to fill missing values for the continuity of data.

269 Upper-air sounding balloons launched at the Zhangjiakou (ZJK) and Beijing
270 Weather Observatory (BWO) sites at 0800 and 2000 local standard time (LST) on 30
271 May 2024 are used to provide the vertical profiles of thermodynamic features, including
272 temperature, pressure, relative humidity, and horizontal winds with a vertical resolution
273 of 5–8 m (Guo et al., 2021b).

274 The meteorological tower with 325 m high is located on 49 m above mean sea level
275 (AMSL). Seven sets of three-dimensional ultrasonic anemometers are installed at seven
276 different heights of the tower: 8, 15, 47, 80, 140, 200 and 280 m, which are used to
277 measure horizontal wind speed, direction, and vertical velocity with a sampling
278 frequency of 10 Hz. These measurements have undergone strict data quality check, and
279 please refer to Shi and Hu (2020) and Shi et al. (2020) for more details.

280 2.2 Radar reflectivity and surface meteorological observations

281 Identification and tracking of the mesoscale convective system (MCS) are
282 conducted using composite radar reflectivity data derived from the China
283 Meteorological Administration (CMA) Doppler radar network. This dataset features a
284 spatial resolution of $\sim 0.01^\circ \times 0.01^\circ$ (latitude \times longitude) and integrates the maximum
285 reflectivity measurements across different vertical levels for each horizontal grid pixel,
286 ensuring comprehensive capture of the MCS's vertical echo structure.

287 For context, the operational CMA Doppler radars employed here have a complete
288 volume scan interval of approximately 6 minutes, which suffices to track the dynamic

Deleted: ; 40.77°N, 114.92°E

Deleted: at 39.97°N, 116.37°E

Deleted: ying

Deleted: is

Deleted: a

Deleted: with a resolution of approximately 0.01° in both latitude and longitude derived

Deleted: It

Deleted: from the Doppler weather radars at each pixel across different levels

299 evolution of the MCS and its associated gust front. To better characterize gust front
300 propagation, radial velocity data from the S-band Doppler radar in BWO are, also used.
301 Ground-based meteorological variables are also used in the analysis over the study
302 area, including 2 m air temperature (T_{2m}), relative humidity, and pressure measured at
303 5 min intervals, as well as instantaneous 10 m wind speed (WS_{10m}), wind direction, and
304 precipitation measured at 1 min intervals from automated weather stations (AWSs).

305 *2.3 Reanalysis and satellite datasets*

306 ERA5 is the fifth-generation atmospheric reanalysis of ECMWF (European Centre
307 for Medium-Range Weather Forecasts), which benefits from advancements in data
308 assimilation, model physics and dynamics (Hersbach et al., 2023). The ERA5 dataset
309 can provide meteorological parameters on 37 pressure level with a spatial resolution of
310 $0.25^\circ \times 0.25^\circ$ at hourly intervals. The geopotential height, temperature, relative humidity,
311 and horizontal wind fields at 500 hPa and 850 hPa are used to analyze the large-scale
312 conditions prior to the severe wind gust event in Beijing.

313 Himawari-8/9 is one of the next-generation geostationary satellites operated by the
314 Japan Meteorological Agency, which was launched on 7 October 2014 and located at
315 $140.7^\circ E$, $0^\circ N$ (Da, 2015). It has provided real-time observations to the public since 7
316 July 2015 (<ftp://ftp.ptree.jaxa.jp/jma>) with diverse central wavelength (from 0.47 to
317 $13.3 \mu m$). Brightness temperature from the $10.8 \mu m$ -channel high-resolution
318 geostationary satellite Himawari-8/9 L1 gridded data with a spatial resolution of 0.25°
319 $\times 0.25^\circ$ (Bessho et al., 2016; Chen et al., 2019) is used in this study to identify and track
320 the MCS at 10-min intervals.

321 *2.4 Calculation of divergence, vorticity, stretching and shearing deformation*

322 Divergence, vorticity, stretching and shearing are four fundamental air motion
323 diagnostics (Yanai and Nitta, 1967; Brandes and Ziegler, 1993, Shapiro et al., 2009).
324 The horizontal divergence D and vertical vorticity ζ respectively reflect the area change
325 and rotation of the air parcel (Lenschow et al., 2007; Beck and Weiss, 2013; Bony and
326 Stevens, 2019). Stretching and shearing deformations, denoted S_1 and S_2 here, result in

Deleted: the propagation of a

Deleted: the

Deleted: Doppler radar

Deleted: is

Deleted: ¶

Deleted: &

Deleted: ; Lenschow et al., 2007

334 elongation parallel to the axis of dilatation and contraction orthogonal to it. Stretching
 335 deformation can flatten and lengthen the air parcel, while shearing deformation can
 336 twist the air parcel in two perpendicular directions.

337 Generally, these four different motions above can be represented by pairs of partial

338 derivatives of velocity $\frac{\partial u}{\partial x} + \frac{\partial v}{\partial y}$, $\frac{\partial v}{\partial x} - \frac{\partial u}{\partial y}$, $\frac{\partial u}{\partial x} - \frac{\partial v}{\partial y}$ and $\frac{\partial v}{\partial x} + \frac{\partial u}{\partial y}$. The triangle method,

339 as proposed by Bellamy (1949), computes the divergence based on the rate of change
 340 in a fluid triangle initially coincident with the network composed by any three points A ,
 341 B , and C . The triangle-area averaged horizontal divergence D and vertical vorticity ζ
 342 can be computed by the triangle method as follows

$$343 \quad D = \frac{(u_B - u_A)(y_C - y_A) - (u_C - u_A)(y_B - y_A) + (x_B - x_A)(v_C - v_A) - (x_C - x_A)(v_B - v_A)}{(x_B - x_A)(y_C - y_A) - (x_C - x_A)(y_B - y_A)}, \quad (1)$$

$$344 \quad \zeta = \frac{(v_B - v_A)(y_C - y_A) - (v_C - v_A)(y_B - y_A) - (x_B - x_A)(u_C - u_A) + (x_C - x_A)(u_B - u_A)}{(x_B - x_A)(y_C - y_A) - (x_C - x_A)(y_B - y_A)}, \quad (2)$$

345 Here, $(x_i, y_i) (i = A, B, C)$ are the location of three vortex points, $\vec{V}_i = (u_i, v_i)$ are
 346 the zonal and meridional component of horizontal wind, respectively.

347 Analogously, the stretching and shearing deformation can be derived using the
 348 following equations:

$$349 \quad S_1 = \frac{(u_B - u_A)(y_C - y_A) - (u_C - u_A)(y_B - y_A) - (x_B - x_A)(v_C - v_A) + (x_C - x_A)(v_B - v_A)}{(x_B - x_A)(y_C - y_A) - (x_C - x_A)(y_B - y_A)}, \quad (3)$$

$$350 \quad S_2 = \frac{(v_B - v_A)(y_C - y_A) - (v_C - v_A)(y_B - y_A) + (x_B - x_A)(u_C - u_A) - (x_C - x_A)(u_B - u_A)}{(x_B - x_A)(y_C - y_A) - (x_C - x_A)(y_B - y_A)}, \quad (4)$$

351 The uncertainties associated with the errors of horizontal wind retrievals, the
 352 spatial scales and the shape of triangles in the calculation of RWP-derived parameters
 353 have been discussed by Guo et al. (2023). To ensure the stability of results, obtuse
 354 angles of more than 140° and areas of less than 500 km² should be avoided for
 355 constructing a reasonable triangle. Here, four triangles from west to east are constructed
 356 based on the positions of six RWPs deployed at YQ, XYL, HR, BWO, PG and SDZ to
 357 meet the consistency in shape and area. It is noteworthy that the value of four dynamic

Formatted: Font: Times New Roman

Deleted: To meet the consistency in shape and area, four triangles from west to east are constructed based on the positions of six RWPs deployed at YQ, XYL, HR, BWO, PG and SDZ....

Formatted: Superscript

Formatted: Superscript

362 parameters is still inversely proportional to the area of triangle as the denominator. This
 363 coincides with the fact that the gradient of velocity between two points will increase
 364 when the distance is shortened. Considering the six RWPs located at different terrain
 365 elevations, the horizontal and vertical velocities measured by each RWP are
 366 interpolated to the same altitude that starts upwards from 0.51 km to 4.95 km above
 367 mean sea level (AMSL) with a vertical resolution of 120 m.

368 2.5 Calculation of frontogenesis function

369 As mentioned above, four air motion types may cause some parts of the air parcel
 370 to move away from each other and some parts of the air parcel to move towards each
 371 other, resulting in frontolysis and frontogenesis respectively (Miller, 1948). Previous
 372 studies have used the frontogenesis function F to infer the evolution of horizontal
 373 temperature gradient (Bluestein, 1986), which contains the following four terms:

$$374 \quad F = \frac{d}{dt} |\nabla_h \theta_e| = F_1 + F_2 + F_3 + F_4, \quad (5)$$

$$375 \quad F_1 = -\frac{1}{2} D |\nabla_h \theta_e|, \quad (6)$$

$$376 \quad F_2 = -\frac{1}{2} \left[S_1 \left(\frac{\partial \theta_e}{\partial x} \right)^2 + 2S_2 \left(\frac{\partial \theta_e}{\partial x} \right) \left(\frac{\partial \theta_e}{\partial y} \right) - S_1 \left(\frac{\partial \theta_e}{\partial y} \right)^2 \right] / |\nabla_h \theta_e|, \quad (7)$$

$$377 \quad F_3 = \left(\frac{\partial \theta_e}{\partial x} \frac{\partial Q}{\partial x} + \frac{\partial \theta_e}{\partial y} \frac{\partial Q}{\partial y} \right) / |\nabla_h \theta_e|, \quad (8)$$

$$378 \quad F_4 = - \left(\frac{\partial \theta_e}{\partial x} \frac{\partial w}{\partial x} + \frac{\partial \theta_e}{\partial y} \frac{\partial w}{\partial y} \right) \frac{\partial \theta_e}{\partial z} / |\nabla_h \theta_e|, \quad (9)$$

379 where ∇_h is the horizontal Hamilton operator, θ_e is equivalent potential temperature, Q
 380 is diabatic heating, w is vertical velocity. The four terms characterize the effects of
 381 horizontal divergence, horizontal deformation, diabatic heating and vertical motion on
 382 frontogenesis. Frontogenesis occurs if F is larger than zero. Since the variability of
 383 vertical velocity along the horizontal direction is quite small, F_4 is not included in the
 384 calculation (Han et al., 2021). D , S_1 and S_2 in the preceding subsection from the RWP
 385 mesonet are then applied to these equations in order to calculate the vertical profile of
 386 F .

Formatted: Font: (Default) Cambria Math, Complex Script
 Font: Cambria Math

387 Limited by the lack of vertical profiles of thermal parameters in real-time, the
 388 gradients of θ_e are obtained from surface observations from AWSs in Beijing. Indeed,
 389 the core drivers of frontogenesis are dynamic processes, while the gradient of θ_e mainly
 390 acts as a scaling coefficient that modulates the efficiency of these dynamic
 391 contributions. This simplification of assuming this "efficiency coefficient" remains
 392 relatively homogeneous in the lower layer is available to capture regions of dynamically
 393 dominated frontogenesis. However, it must be acknowledged that surface observations
 394 may not adequately represent baroclinic structures aloft, especially in the presence of
 395 temperature inversion or strong vertical shear. Consequently, the diagnostic results are
 396 most applicable to near-surface environments and shallow frontogenesis. Future
 397 improvements would benefit from incorporating vertically resolved thermal variables
 398 obtained from operational high-frequency detection (e.g., microwave radiometers) for
 399 a more comprehensive assessment.

Formatted: Indent: First line: 2 ch

Formatted: Font: Times New Roman, Not Italic, Complex Script Font: Not Italic

Formatted: Font: Times New Roman, 12 pt, Not Italic, Complex Script Font: 12 pt, Not Italic

Formatted: Font: Times New Roman, 12 pt, Not Italic, Complex Script Font: 12 pt, Not Italic

Formatted: Font color: Auto

400 2.6 Identification of inverse energy cascade

401 The direction of the turbulent energy cascade is determined by the sign of the
 402 energy flux ε , which is calculated based on the third moment of the velocity difference
 403 (Shao et al., 2022):

$$404 \varepsilon = -\frac{2}{3} \left\langle \frac{[u_r(x+r) - u_r(x)]^3}{r} \right\rangle, \quad (10)$$

405 where r is the distance along any direction, u_r is the velocity parallel to r , and the
 406 angular bracket denotes the ensemble mean. Based on Taylor's hypothesis (Taylor, 1938;
 407 Powell and Elderkin, 1974), the pattern of turbulence can be considered to be "frozen"
 408 as it advects past a sensor. This allows the conversion of spatial measurements into
 409 temporal observations at a fixed point. When applying Eq. (10) in the zonal direction,
 410 it can be rewritten as:

$$411 \varepsilon = -\frac{2}{3} \left\langle \frac{[u(t+\Delta t) - u(t)]^3}{u(t)\Delta t} \right\rangle, \quad (11)$$

412 where $u(t)$ is the zonal component of horizontal wind speed derived from the three-
 413 dimensional ultrasonic anemometer at any time t . Δt denotes the time interval between

Formatted: Font: Times New Roman

Formatted: Font: Times New Roman

Deleted: vertical

Deleted: as

Formatted: Font: Times New Roman

Deleted:
$$\varepsilon = -\frac{2}{3} \left\langle \frac{[w(z+\Delta z) - w(z)]^3}{\Delta z} \right\rangle$$

Formatted: Font: Times New Roman

Formatted: Font: Times New Roman

Formatted: Font: Times New Roman

Field Code Changed

Deleted: w

Deleted: vertical

Deleted: velocity

Deleted: one

Deleted: height

Deleted: z

Deleted: height difference

Formatted: Font: Italic, Complex Script Font: Italic

424 two consecutive observations. Positive and negative ε indicate direct and inverse energy
425 cascade (IEC), respectively. IEC is generally identified when $\varepsilon < -0.002 \text{ m}^2 \cdot \text{s}^{-3}$ to
426 minimize the impact of observational errors on the results (Zhou et al., 2025).

Deleted: the upper height and z

427 3. Case overview

Deleted: ¶

428 In the afternoon of 30 May 2024, an extreme wind event occurred as a MCS,
429 propagated eastward and entered the plain. Figure 2 shows the Himawari-8 $10.8 \mu\text{m}$
430 brightness temperature, superimposed with mosaic composite radar reflectivity during
431 the different stage. During the evolution of the MCS, a number of high winds
432 (instantaneous 10 m wind speed $\geq 17.2 \text{ m s}^{-1}$) were observed by automatic weather
433 stations in Beijing after 1330 LST (Fig. 3a). What we focus on is that high winds
434 became more widespread in the western mountainous areas of Beijing from 1400 to
435 1429 LST (Fig. 3b) during the downhill progress of the developing MCS (Fig. 2b-d),
436 with the maximum instantaneous 10 m wind speed of 37.2 m s^{-1} detected at the Qianling
437 Mountain site. After 1430 LST, both rainfall and the number of stations recording high
438 winds increased remarkably (Fig. 3c) associated with the merger of two convective
439 segments and formation of the squall line, at around 1436-1448 LST (Fig. 2e, f). The
440 squall line further consolidated and reached its mature stage after 1500 LST, defined
441 by the fully coherent, organized linear structure (Fig. 2g, h). The wind gust coincided
442 with the intensification of deep convection with the peak rainfall exceeding 9 mm
443 during 1500-1529 LST along the leading line (Fig. 3d), after which the squall line
444 moved eastward away from the major urban area of Beijing.

Deleted: a

Deleted: downhill thunderstorm

Deleted: the MCS

Deleted: 2a

Deleted: High

Deleted: mainly occurred

Deleted: (Fig. 2b)

Deleted: (39.87°N, 116.07°E)

Deleted: 2c

Formatted: Font: Times New Roman

Deleted: At the mature stage of squall line (Fig. 2d), t

Formatted: Font: Times New Roman

Deleted: maximum

445 3.1 Synoptic background

446 Figure 4a-b shows the large-scale conditions at 1300 BJT prior to the extreme wind
447 gust event. Significant cold advection with the northwesterly jet exceeding 20 m s^{-1} was
448 found over Beijing that was associated with a deep northeast cold vortex at 500 hPa.
449 Meanwhile, Beijing was situated in the warm sector with temperature exceeding 15°C
450 at 850 hPa (Fig. 4b). The steep midlevel lapse rate of temperature provides a favorable
451 environment for deepening organization of convection and releasing unstable energy.

Deleted: 3a

Deleted: 3b

467 A short-wave trough at 850 hPa, located to the west of Beijing (Fig. 4b), likely
468 contributed to synoptic-scale lifting ahead of the trough axis. The associated ambient
469 wind shear offered a key dynamic ingredient for the subsequent deepening organization
470 of convection.

471 Unfortunately, no sounding was available to elucidate the temporal evolution of
472 thermal stratification during the gusty wind event. We can only indicate the pre-storm
473 environment by the soundings at 0800 LST from the radiosonde at the ZJK and BWO
474 sites shown in Figs. 4c and 4d, respectively. Consistent with the ERA5 reanalysis data,
475 the sounding at the ZJK revealed upstream conditions in which thunderstorms were
476 likely to develop (Fig. 4c). These conditions consist of a strong northwesterly wind
477 oriented perpendicular to the Mt. Taihang range at middle level, accelerating the
478 downhill process of storm (Wilson et al., 2010; Chen et al., 2012; 2014; Li et al., 2017;
479 Xiao et al., 2017; 2019; Guo et al., 2024). The potential for terrain-triggered gravity
480 waves in the leeside that can modulate localized uplift and cloud organization (Neiman
481 et al., 1988; Lombardo and Kumjian, 2022; Rocque and Rasmussen, 2022).

482 The veering of the northerly wind to a westerly wind from 850 hPa to above 400
483 hPa also indicated the presence of cold advection at the BWO. The Skew T-logP
484 diagram at the BWO shows moderate convective available potential energy (CAPE) of
485 460.5 J kg^{-1} and convective inhibition (CIN) of 114.4 kg^{-1} . A deep dry layer was seen
486 from the surface to about 350 hPa with low-level humidity less than 60%. This dry
487 column provided a favorable environment for the evaporation of precipitation particles
488 from the moving storm. The evaporative cooling might have enhanced cold downdraft
489 air, potentially contributing to the generation of the wind gust event. After the passage
490 of the MCS, a surface-based temperature inversion layer below 880 hPa with larger
491 CIN was captured by the sounding at 2000 LST (not shown) as a result of the rapid
492 decrease in surface temperature.

493 3.2 Evolution of the QLCS

494 At the same time, the evolution of 30-minute perturbations of T_{2m} (ΔT_{2m}),
495 superimposed with 30-minute perturbations of pressure (ΔP), is displayed in Fig. 5. It

Deleted: A short-wave trough with horizontal wind shear appeared to the west of Beijing at 850 hPa (Fig. 3b), indicating the important dynamic contribution to the subsequent deepening organization of convection.

Deleted: 3c

Deleted: 3d

Deleted: 3c

Deleted: mountaintop

Moved (insertion) [5]

Deleted: ; Xiao et al., 2017; 2019; Li et al., 2017; Wilson et al., 2010

Moved up [5]: (Chen et al., 2012; 2014; Guo et al., 2024; Xiao et al., 2017; 2019; Li et al., 2017; Wilson et al., 2010)

Deleted: increasing with height and oriented perpendicular to the Mt. Taihang range throughout a deep layer

Deleted: ¶

Deleted: is

Deleted: intense

Deleted: have

Deleted: d

Formatted: Not Highlight

Deleted: thus leading to

Deleted: After the passage of the MCS, a surface-based temperature inversion layer below 880 hPa with larger CIN was captured by the sounding at 2000 LST due to the heat release (not shown).

Deleted: Westerly winds controlled the near-surface layer and gradually changed upward to northwesterly at 700 hPa, implying some warm advection in some degrees.

Deleted: Figure 4 shows the Hiamwari-8 $10.8 \mu\text{m}$ brightness temperature, superimposed with mosaic composite radar reflectivity during the different stage of the QLCS.

526 is evident from Fig. 2a that relatively dry conditions and few clouds covered much of
527 the plain in the early afternoon of 30 May. Furthermore, the plain was dominated by a
528 surface south-to-southwesterly flow (Fig. 5a). A circular-shaped cloud cluster with
529 more intense convective activity, denoted as C1, propagated eastward and then the front
530 of convection approached the western section of the RWP mesonet until 1400 LST (Fig.
531 2b). One can see rising pressure at the rate of more than 4 hPa in 30 minutes with a
532 strengthening cold pool at the center with a cooling rate of more than 10 °C 30min⁻¹
533 associated with the main area of the MCS (Fig. 5b). The dry subcloud air (Fig. 4c, d)
534 was one of the factors that facilitated cold pool consolidation and rapid organization of
535 convection.

Deleted: 4a

Deleted: 4b

Deleted:

Deleted: 4c

536 It's clearly shown in Figs. 2c and 5c that stronger thunderstorms persisted at 1412
537 LST with convectively generated cold air. Of particular relevance to this study is the
538 emergence of a convective line near 39.7°N, 115.6°E at the leading edge of the cold
539 outflows (Fig. 5c). This convective line formed from the low-level convergence as the
540 north-to-northeasterly cold outflows met westerly winds to the south, which appeared
541 to help initiate convection cells to the west of the plain line. Shortly after, explosive
542 convection emerged (Fig. 2d) along the convective line (Fig. 5d) as the outflow
543 boundary entered the plain at 1424 LST, indicating the potential for heavy precipitation
544 aloft. However, it is noteworthy that only light precipitation appeared to reach the
545 ground prior to 1430 LST with rainfall rate less than 3mm 30min⁻¹ (Fig. 3b). The weak
546 measured rainfall was consistent with low reflectivity at the elevation angle of 0.5°
547 from the S-band Doppler weather radar at BWO (not shown). This further confirmed
548 that a pronounced dry layer in the low level caused significant sublimation, melting,
549 and evaporation of precipitation particles. The evaporative cooling effect of
550 precipitation particles likely fostered the development of evaporatively cooled air that
551 expanded rapidly over the western mountain region, as mentioned before.

Formatted: Font: Times New Roman

Deleted: 4d

Deleted: 2b

Deleted: !

Deleted: , as mentioned before

552 Furthermore, the distinct local wind maximum was attributed partly to the venturi
553 effect by canyon in accelerating the instantaneous wind speed. Many long and narrow
554 valleys exist at the junction of the southern foothill of Mt. Yan and the eastern foothill

563 of Mt. Taihang, which can be seen in Fig. 1. Northwest cold air rapidly accelerated and
564 swept across downstream areas after being funneled through canyons and mountain
565 passes (Smith, 1979; Grubišić et al., 2008). It is well known that Santa Ana winds with
566 gusts exceeding 100 km h^{-1} is closely connected with the channels over the Sierra
567 Nevada and Transverse Ranges (Guzman-Morales et al., 2016; Prein et al., 2022),
568 destroy crops and greatly create the spread of wildfires for centuries (Kelley et al.,
569 2025). In addition, lower surface roughness in the mountainous areas also results in
570 higher 10-m wind speeds (Barthelmie, 2001; Luu et al., 2023), especially when the dry
571 environment is unfavorable for vegetation growth, while urban buildings increase
572 frictional drag and surface roughness length z_0 values over a city (Oke, 1987).

Deleted: Grubisic

Deleted: ; Smith, 1979

Formatted: Superscript

573 At 1330 LST, a leading stratiform region consisting of several dispersed
574 convective cells, denoted as C2, was located to the north of the mesonet (c.f. Fig. 2a).

Deleted: this time

Deleted: 4a

575 The convection cell near HR maintained and developed rapidly in coverage and
576 intensity from 1400 to 1424 LST (Fig. 2b-d) due to the persistent convergence of low-

Deleted: 4b

577 level southerly flows at the foot of Mt. Yan (c.f., Fig. 5b-d). This coincided with a
578 surface cold pool with T_{2m} drops as large as 6°C in 30 minutes. After 1436 LST, it
579 gradually merged with the southern convective segment as mentioned above and
580 strengthened to an intense and well-organized squall line that had a nearly contiguous

Deleted: 4e

581 reflectivity region of 35 dBZ at least 150 km in length (Fig. 2e and f). The southern
582 convective line significantly extended after intersecting with the preexisting
583 convergence zone at the foothills of Mt. Yan (Fig. 5e and f). Apparently, the appearance
584 of secondary maximum 10 m wind speed area in Fig. 3c coincided with the

Deleted: 2c

585 intensification of the gust front, as evidenced by its increased width and echo intensity.
586 The continuous increasing of rainfall (c.f. Fig. 3c) in triangle 1 and 2 resulted in a
587 distinct cold center at the cooling rate of more than 12°C .

Deleted: 2c

588 The squall line subsequently developed a larger-scale bow echo (Fujita 1978) and
589 accelerated to the east-southeast as the system became oriented more perpendicular to
590 the mean northwest wind in the middle troposphere (Fig. 2g, h). The QLCS
591 subsequently moved eastward with the leading convective line and a trailing stratiform

Deleted: 4g

601 region during the mature stage (Fig. 2g, h), which are similar to the asymmetric
602 archetype of a squall line found by Johnson and Hamilton (1988) and Zhang et al.
603 (1989). The midlevel rear-inflow jet (RIJ) that feeds into the stratiform region of
604 QLCs plays an important role in producing the high winds at the surface (Weisman
605 and Davis, 1998; Xu et al., 2024), which has also occurred in the present case, as shown
606 in the next subsection.

Deleted: 4g

Deleted: &

607 4. Vertical Structures of the Gusty Winds

608 4.1 Horizontal Divergence and Vertical Vorticity Analyses

609 In the preceding section, the synoptic-scale weather system was shown to be
610 favorable for stronger convection with evidently identifiable boundaries of the 30 May
611 2024. Here, the localized environmental conditions are analyzed for forcing
612 mechanisms supporting the advancing regeneration of convection along the leading line
613 and associated winds. To gain insight into the fine-scale structures of this extreme wind
614 gust event, we calculated the height-time cross sections of horizontal winds and vertical
615 motion from the RWPs during 1300-1530 LST on 30 May 2024. Figure 6 presents the
616 vertical distribution of vertical vorticity (ζ) and horizontal divergence (D) within
617 triangular regions calculated from Equations 1 and 2, together with the evolution of the
618 95th percentile of the 10-m wind speed. The 95th percentile was selected rather than the
619 maximum value to provide a more robust representation of the overall distribution.

620 Before the MCS reached Beijing, sustained low-level south-to-southwesterly wind
621 was observed in the lowest 1.5 km layer in the early afternoon of 30 May 2024 from
622 seven RWP stations (not shown), accompanied by weak near-surface convergence in
623 the main plain area (Fig. 6b-d). Especially, more noticeable convergence in the lower
624 to mid-troposphere was detected locally over triangle 3 after 1300 LST (Fig. 6c) by the
625 uplifting along the foothills of Mt. Yan. Divergence below 4 km AMSL in triangle 1
626 could to a certain extent be influenced by the valley flows at the foot of the Taihang
627 mountains (Fig. 6a). As the main convective element C1 propagated eastward, an
628 evident increase was observed in horizontal convergence in the lowest 2 km AMSL

631 layer along the leading line of the strengthening cold pool after 1342 LST (Fig. 6a, b).
632 The convergence and associated updraft increased in amplitude and deepened rapidly,
633 which resulted in the generation of clouds and convective cells along the downshear
634 side of the cold pool that expanded south and east after 1400 LST (c,f. Fig. 2b-d). The
635 presence of divergence aloft above near-surface convergence layer confirmed the
636 development of this deep, organized convection that played an important role of
637 generating the potential precipitation. It created favorable conditions for the
638 evaporative cooling to accelerate the enhancement of the cool pool. The intense cold
639 pool, in turn, was the primary driver for high winds through the downward momentum
640 transport and pressure gradient forcing (Houze, 2014; Haerter et al., 2019; Hadavi and
641 Romanic, 2024), which will be further examined in Section 4.2.

Deleted: 4b

Formatted: Font: Times New Roman

Formatted: Font: Times New Roman

642 Of importance to note is the rapid growth of surface-based positive vorticity over
643 triangle 2 coupled with intense convergence across the gust-frontal zone during the
644 passage of the main convective element. A deep layer of cyclonic vorticity was detected
645 in the lower half of the troposphere over triangle 2 with the maximum value of $-2.8 \times$
646 10^{-4} s^{-1} centering near 3 km AMSL at 1436 LST. The strongest surface wind speed at
647 the 95th percentile appeared nearly in phase after the peak of cyclonic vorticity, as also
648 shown in Fig. 6b. These structures are similar to those shown by Zhang (1992),
649 suggesting that the moderate positive ζ was generated through upward vortex stretching
650 ahead of convection, whereas the large negative ζ , likely located behind, resulted from
651 the downward stretching of moderate negative (absolute) ζ . Weisman and Trapp (2003)
652 found that mesoscale vortices may be responsible for the production of damaging
653 straight-line winds by notably modifying the local outflow and determining the location
654 of the wind speed maximum.

655 The northeastern dispersed convective cores with radar reflectivity more than 35
656 dBZ were completely separated from the major convective segment to the south and
657 remained closely related to the convergence of southwesterly flows over triangle 3 (Fig.
658 5c), like the counterpart of surface streamline shown in Fig. 2. The surface-based
659 convergence strengthened over triangle 3 and 4 after 1400 LST, with divergence above

Deleted: 6c

Deleted: 4.

663 (Fig. 6c, d) in the absence of significant local evaporative cooling. After merging with
664 the main area convection which moved across the plain line in the urban region after
665 1436 LST, a deep layer of convergence and intense upward motion above 5 km AMSL
666 over triangle 3 and 4 tended to enhance the squall line (Fig. 6c and d), leading to heavy
667 rainfall (Fig. 3c). We may speculate that the low-level cyclonic vorticity of $1.8 \times 10^{-4} \text{ s}^{-1}$
668 ¹ (i.e., centered at 1-km altitude) after 1436 LST coincided with the development of the
669 area-averaged convergence during the periods, similar to that captured by triangles 2.
670 Moreover, the intersection of two segments formed a pivot point in triangle 3 (Fig. 2f)
671 for the change in line orientation and marked the area of mesovortices under study.
672 Both the area and intensity of the observed high winds increased remarkably during
673 this hour (Fig. 6c), with the most severe winds over 30 m s^{-1} and significant property
674 damage occurring in the merger region (Fig. 3c). The development of a large, intense
675 MCS resulted from a complex series of processes and mergers of several convective
676 lines and clusters over a relatively short time period, which is also common for warm
677 season MCSs (French and Parker; 2012).

678 Note a deep layer of strengthening cyclonic vorticity above 4 km AMSL
679 dominated triangle 3 and 4 after the merger (Fig. 6c, d) and gradually extended
680 downward to the altitude of 3 km with the center value exceeding $2.8 \times 10^{-4} \text{ s}^{-1}$. It
681 suggested that the midlevel rotation of the frontal vortex played an important role in
682 enhancing the elevated RIJ, similar to the enhancement of near-surface high winds by
683 the low-level rotation. The strongest winds tended to occur on the southwestern side of
684 the mesoscale vortices where the ambient translational northwesterly flow and the
685 mesoscale vortices' rotational flow were in the same direction (e.g., Wakimoto et al.
686 2006; Xu et al. 2015b). The intensification of the RIJ were possibly attributed to the
687 locally enhanced cold pool with the increased rainfall in the merger area (c.f. Fig. 3).

688 Simultaneously, the lower-tropospheric convergence in triangle 1 and 2 started
689 showing a decreasing trend, followed by large negative ζ in descending rear inflows. In
690 addition, the surface wind speed diminished dramatically with significant divergence
691 in the lowest 2-km layer shortly (i.e., between 1500 and 1530 LST) after the passage of

Deleted: 2c

Deleted: 2c

Deleted: Atkins and St. Laurent 2009;

Deleted: 2

696 the gust front. The changeover to divergence was likely driven by evaporative cooling
697 of raindrops, as evidenced by the emergence of outflows behind the leading convective
698 line, which could also to a certain extent be influenced by downslope flows over the
699 western mountains. One may note the presence of elevated, much weaker convergence
700 centered at 3 km. This could be attributed to the approach of trailing stratiform
701 precipitation, as indicated by Houze et al. (1989) and Zhang and Gao (1989) in their
702 respective observational and modeling studies of squall lines.

Deleted: (c.f. Figs. 11b and 12e, f)

703 4.2 Vertical Momentum Transport

Moved (insertion) [1]

Deleted: 3

704 Apparently, the passage of the wind gust resulted in significant alterations to the
705 vertical profiles and intensity of the above fields. Specifically, weaker southwest-to-
706 westerly flows with wind speed less than 8 m s^{-1} up to 1.5 km AMSL were detected by
707 the RWP at HD prior to the arrival of the gust front (Fig. 7a) from the height-time cross
708 section of horizontal winds. Meanwhile, the northwesterly jet exceeding 15 m s^{-1}
709 controlled the higher altitude above 3 km AMSL. Evidently, such an intense gust front
710 was related to the critical influence that substantial vertical wind shear exerts on
711 convection. Then, sharp wind directional shifts to northwesterly happened with
712 increasing 10 m wind speeds from less than 5 m s^{-1} to more than 10 m s^{-1} in the lowest
713 1-km layer at 1436 LST. The intense northwest-to-northerly winds with strong
714 descending motion coincided with the occurrences of light rainfall with the total
715 accumulation of about 5 mm (Fig. 7a), pronounced surface temperature drops and
716 pressure rising (Fig. 7b). The effect of light precipitation on the radar measurement was
717 neglected because the fluctuating component of the horizontal velocity was much larger
718 in magnitude. The precipitation was just concentrated near 1442 LST and decreased
719 rapidly to less than 1 mm per 6 minutes shortly thereafter. Given that the weak
720 precipitation ended by 1500 LST, the vertical velocity associated with the squall line
721 (i.e., -8 m s^{-1} shown in Fig. 7c) represented the intensity of evaporatively induced
722 downdrafts rather than the falling speed of the raindrops.

Deleted: 8

Formatted: Font: Times New Roman

Deleted: 8

Deleted: 8

Deleted: 8

723 Previous studies have used the horizontal momentum budget equation to diagnose
724 the contribution of each term in momentum transport within MCSs, mostly in modeling

731 studies (Mahoney et al., 2009; Mahoney and Lackmann, 2011). To investigate the roles
732 of internal circulations of the MCS in producing the present wind gust event, the
733 vertical momentum transport of zonal wind, $-w\partial u/\partial z$ was estimated. Figure 8c shows
734 enhanced near-surface positive tendencies of the vertical advection at HD below 1 km
735 AMSLL ahead the gust front. In response to the forcing of the QLCS, the elevated RIJ
736 occurring in the western portion of the mesovortex after 1436 LST corresponded well
737 to the vertical structure observed by the RWP mesonet in subsection 4.1. The RIJ was
738 also amplified by developing downdrafts behind the gust front with the maximum value
739 more than -8 m s^{-1} near 1500 LST. The accelerated downward transport of high
740 momentum associated with the RIJ produced intensified high winds of over 25 m s^{-1}
741 below 1 km AGL (Fig. 7a) at 1512 LST. Thus, we may state that the above evidence is
742 further indicative of the important roles of downward momentum transport with the
743 descending rear inflows in generating the damaging wind event under study.

744 *4.3 Deformation and Frontogenesis Analysis*

745 To the forecaster, the most significant aspects of a frontal zone are the cloudiness
746 and convection that are usually associated with it. Horizontal convergence and
747 deformation fields are two key mechanisms that drive frontogenesis by concentrating
748 temperature gradients and enhancing frontal sharpness. Figures 8a shows the evolution
749 of the frontogenesis function and shearing deformation as described in subsection 2.4
750 and appeared to depict this frontogenesis event in the low-level layer. Both stretching
751 and shearing deformation cause some parts of the air parcel moving towards each other
752 and result in weather fronts. Shearing deformation was positive associated with the air
753 parcel stretching in the southwest/northeast direction and contracting in the
754 southeast/northwest direction. Convection developed along this feature as it moved
755 north and east. Likely aiding the convective development was the strong horizontal
756 convergence and low-level deformation frontogenesis. This conclusion is supported by
757 the fact that the squall line aligned with the long axis of the frontogenesis (Fig. 2e-h).

758 Triangle 1 and 2 experienced weak frontogeneses in the lowest 1.5 km layer before
759 the arrival of the southeast segment (c.f. Fig. 8a, b). As the horizontal convergence

Deleted: &

Deleted: ; Mahoney et al., 2009

Deleted: 8

Deleted: ¶

Deleted: 2

Deleted: 7a

Deleted: 4e

Deleted: 7a

768 increased, frontogenesis was strengthened after 1330 LST up to the middle altitude of
 769 3 km with a peak value of $4.8 \times 10^{-8} \text{ K m}^{-1} \text{ s}^{-1}$ near 1.5 km AMSL at 1424 LST over
 770 triangle 1. The convergence contributed to the compression of the temperature gradient
 771 and promoted the strong concentrated sloping updraft occurring on the warm side of
 772 the region of maximum geostrophic compression of the isotherms. This mesoscale
 773 circulation closely resembles the flow in a mesoscale precipitation band analyzed by
 774 Emanuel (1985), Bosart and Sanders (1981). Cold outflows associated with
 775 evaporatively driven moist downdrafts were evident, with the continuous cooling rate
 776 of about 15 K h^{-1} by 1500 LST in triangle 1 and 2 (Fig. 8a, b). By contrast, a sharp drop
 777 of area-averaged θ_e in triangle 3 was generated by significant rainfall which took place
 778 in the merger stage (Fig. 8c). The warming pattern was observed in triangle 2 with rising
 779 θ_e , which was possibly attributed to the dry subsidence warming associated with the
 780 descending RIJ at the back edge of the precipitation region.

781 4.4 Turbulent Kinetic Energy Transfer

782 As the well-sustained mesoscale convection created a favorable dynamic
 783 environment for the evolution of small-scale turbulent processes, the interaction
 784 between the organized squall system (and its embedded mesovortex and rear-inflow jet)
 785 and the ambient flow laid the foundation for the subsequent intensification of turbulent
 786 energy transfer, which is essential for the evolution of severe convective gust and
 787 related convective activities (Adler and Kalthoff, 2014; Dai et al., 2014; Dodson and
 788 Griswold, 2021; Su et al., 2023). Understanding mechanisms of the turbulent kinetic
 789 energy (TKE) transferring in the PBL between the surface and atmosphere is crucial for
 790 turbulence parameterization in numerical models, especially for extreme wind events
 791 (Powell et al., 2003; Monahan et al., 2015; Lyu et al., 2023).

792 In contrast to the Monin-Obukhov similarity theory that TKE transfers from larger
 793 to smaller eddies until it is dissipated at the smallest scales (Kolmogorov, 1941; Monin
 794 and Obukhov, 1954), many studies discovered the phenomenon of inverse energy
 795 cascades (IEC) in a totally different way (Kraichnan, 1967; Byrne and Zhang, 2013;
 796 Tang et al., 2015). Despite these advances in theoretical and numerical studies,

Deleted: 7a

Formatted: Font: Italic, Complex Script Font: Italic

Deleted: 7c

Moved up [1]: 4.3 Vertical Momentum Transport

Apparently, the passage of the wind gust resulted in significant alterations to the vertical profiles and intensity of the above fields. Specifically, weaker southwest-to-westerly flows with wind speed less than 8 m s^{-1} up to 1.5 km AMSL were detected by the RWP at HD prior to the arrival of the gust front (Fig. 8a) from the height-time cross section of horizontal winds. Meanwhile, the northwesterly jet exceeding 15 m s^{-1} controlled the higher altitude above 3 km AMSL. Evidently, such an intense gust front was related to the critical influence that substantial vertical wind shear exerts on convection. Then, sharp wind directional shifts to northwesterly happened with increasing 10 m wind speeds from less than 5 m s^{-1} to more than 10 m s^{-1} in the lowest 1-km layer at 1436 LST. The intense northwest-to-northerly winds with strong descending motion coincided with the occurrences of light rainfall with the total accumulation of about 5 mm (Fig. 8a), pronounced surface temperature drops and pressure rising (Fig 8b). The effect of light precipitation on the radar measurement was neglected because the fluctuating component of the horizontal velocity was much larger in magnitude. The precipitation was just concentrated near 1442 LST and decreased rapidly to less than 1 mm per 6 minutes shortly thereafter. Given that the weak precipitation ended by 1500 LST, the vertical velocity associated with the squall line (i.e., -8 m s^{-1} shown in Fig. 8c) represented the intensity of evaporatively induced downdrafts rather than the falling speed of the raindrops.

Previous studies have used the horizontal momentum budget equation to diagnose the contribution of each term in momentum transport within MCSs, mostly in modeling studies (Mahoney & Lackmann, 2011; Mahoney et al., 2009). To investigate the roles of internal circulations of the MCS in

Deleted: ring

Formatted: Font: Times New Roman

Deleted: ; Monahan et al., 2015; Powell et al., 2003

Deleted: &

Deleted: &

Deleted: Kraichnan, 1967;

887 observational support for IEC in the atmosphere remains insufficient (Shao et al., 2023a;
 888 2023b). This study further examined the direction of the energy cascade associated with
 889 wind gusts using three-dimensional ultrasonic anemometers at seven heights, denoted
 890 as z_1 to z_7 , on the meteorological tower in Beijing. According to Eq.(11), we can detect
 891 the occurrence of IEC at each height in every moment with a time resolution of 0.1 s.
 892 The frequency of IEC during a period was evaluated as the ratio of the number of
 893 time-height grids identified as IEC to the total number of samples. In this way, we got
 894 height-resolved occurrence frequency of IEC for the study period in Fig. 9a. It is shown
 895 that IEC is a more prevalent phenomenon within the near-surface wind field. Notably,
 896 the frequency and intensity of IEC at all heights increased significantly when near-
 897 surface wind speeds exceeded 10 m s^{-1} . The frequency of IEC reaches up to 45% after
 898 1436 LST, indicating that strong winds are contributed to IEC. The result in Figure 9b
 899 and c revealed that the power spectral density (PSD) was higher after 1436 LST in the
 900 lower-frequency area, especially for the u and v directions, which confirmed the activity
 901 of turbulent kinetic energy from smaller to larger eddies.

902 The observed surge in the frequency of IEC during the passage of convective
 903 outbreak suggests a temporary reorganization of turbulent energy transferring. These
 904 features are similar to those proposed by the observational analyses in two-dimensional
 905 turbulence (Shao et al., 2022; Zhou et al., 2025), which revealed that the formation of
 906 rapid rotation is a crucial driver of IEC. Strong horizontal shear generated by the gust
 907 front likely imposes a quasi-two-dimensional constraint on the flow, suppressing the
 908 three-dimensional vortex-stretching mechanism that normally drives a forward cascade.
 909 In this regime, enstrophy (the square of vorticity) may become partially conserved. Just
 910 as vigorously stirring the water in a very shallow pond causes small swirls to merge
 911 into a single, large vortex, a massive storm can be seen as the end product of an inverse
 912 cascade, where energy from small-scale convection organizes into a giant, coherent
 913 vortex. Another possible explanation is that the rapid increase in wind speed abruptly
 914 shifts the Reynolds number, possibly triggering transient instabilities that further
 915 promoted the generation of quasi-two-dimensional vortex (Browand and Winant, 1973).

Deleted: ,

Deleted: Shao et al.,

Formatted: Not Highlight

Deleted: According to Eq.(11), the energy flux can only be obtained at six heights (from z_1 to z_6) by the differences of vertical velocity ($w_2-w_1, w_3-w_2, \dots, w_7-w_6$) between two adjacent heights. Therefore, there were six samples to identify IEC for every moment.

Deleted: IEC

Deleted: 50

Deleted: These

Deleted: s

Deleted: were

Deleted: 2D

Deleted: suggested

Formatted: Font: Times New Roman

Formatted: Font: Times New Roman

930 The amplification of large-scale eddies transfer momentum downstream more
931 efficiently and enhance wind gusts as a form of positive feedback. In addition, the
932 reduction of surface drag coefficient under robust weather systems impedes the
933 dissipation of energy throughout the boundary layer, prolonging the duration of high
934 winds (Raupach, 1994; Mahrt et al., 2003; Powell et al., 2003).

935 This event illustrates how synoptic-scale disturbances can locally override the
936 classical theory of energy dissipation, leading to a measurable, height-dependent
937 signature of IEC in the PBL. In turn, this shear-driven IEC likely played a catalytic role
938 in consolidating the storm's low-level circulation, demonstrating how microscale
939 turbulent processes can feedback on the mesoscale storm organization. These findings
940 provided favorable evidence for the unique features of 2D turbulence in high wind
941 conditions. These findings have implications for turbulence parameterizations in
942 numerical weather prediction and climate models. Future research should further
943 investigate the mechanisms driving the formation of IEC in more detail and explore the
944 potential link between IEC and different meteorological phenomena.

945 5. Concluding remarks and summary

946 The complex evolution of convective systems crossing mountainous terrain, and
947 associated damaging surface winds, represent a substantial forecasting challenge. In
948 this study, a convectively generated gust wind event by a QLCS that occurred in Beijing
949 during the early afternoon of 30 May 2024 is examined. Beijing's intricate topography,
950 introduces inherent complexity to convective organization during the downhill
951 thunderstorm propagation, facilitating the development of extreme wind gusts. To
952 document the complexity of the convective event's development and evolution, the
953 dynamical characteristics of multiscale processes are explored by utilizing a high-
954 resolution mesonet comprising seven RWPs, a meteorological tower, automated
955 surface stations, radar and satellite data. A conceptual model illustrating the observed
956 dynamical structures and multi-scale processes responsible for this Beijing extreme
957 gust event is presented in Fig. 10.

Deleted: The amplification of large-scale eddies transfer momentum to the surface more efficiently and enhance wind gusts as a form of positive feedback, corresponding with stronger low-level wind speeds and gusts.

Moved up [4]: The amplification of large-scale eddies transfer momentum to the surface more efficiently and enhance wind gusts as a form of positive feedback, corresponding with stronger low-level wind speeds and gusts. These findings provided favorable evidence for the unique features of 2D turbulence in high wind conditions. Future research should further investigate the mechanisms driving

Deleted: the reduction of surface drag coefficient under ... [5]

Deleted: represents

Deleted: with the extreme winds, which

Deleted: The

Deleted: of Beijing

Deleted: provides

Deleted: in

Deleted: the

Deleted: cess

Deleted: leading to

Deleted: the

Deleted: development and evolution of the

Deleted: the

Deleted: ed of

Deleted: radar wind profilers (

Deleted:)

Deleted: (AWSs)

Deleted: for

Deleted: dynamical

Formatted: Font: 12 pt, Not Bold, Complex Script Font: 12 pt

Formatted: Font: 12 pt, Not Bold, Complex Script Font: 12 pt

Formatted: Font: 12 pt, Not Bold, Complex Script Font: 12 pt

Deleted: before and after merger of this QLCS

Deleted: given

1016 Before the merger of the QLCS (Fig. 10a), the northern convection portion
 1017 maintained and developed rapidly due to the convergence of southerly winds along the
 1018 southern slopes of Mt. Yan. Meanwhile, a convergence line formed at the boundary of
 1019 convectively generated cold outflows, mostly associated with the southern portion.
 1020 During the downhill process, the environmental southerly winds in the near-surface
 1021 layer facilitated efficient storm-relative inflow of highly unstable air, supporting the
 1022 continued regeneration of strong convection along the advancing cold pool, where a
 1023 very large area of nearly contiguous radar reflectivity echoes greater than 45 dBZ was
 1024 concentrated over the foot of western mountains. The presence of pronounced
 1025 convergence from the PBL in updrafts led to the rapid intensification of surface-based
 1026 cyclonic vorticity through vertical stretching during the early stages. Evaporative
 1027 cooling enhanced the generation of the extreme winds via downward momentum
 1028 transport and pressure gradient forcing.

1029 As shown in Fig. 10b, the two convective segments merged into a well-organized
 1030 squall system, moving perpendicular to the mean deep-layer wind/shear and developing
 1031 a larger-scale bow-echo structure after reaching the plain. In the merger stage, a
 1032 midlevel layer of intense cyclonic vorticity favored the development of RIJ behind the
 1033 precipitation area, driven by the superposition of ambient flow and the rotational flow
 1034 on the west side of the mesovortex. The calculation of the zonal momentum budget
 1035 further confirmed the importance of horizontal momentum downward transport in
 1036 accelerating lower-level flows within the descending RIJ.

1037 Large-scale analyses show that the deep, well-mixed PBL with very steep lower-
 1038 tropospheric lapse rates and conditional instability provided a favorable background for
 1039 consolidating the dispersed multicell thunderstorm. The emergence of pronounced low-
 1040 level frontogenesis, coupled with significant shearing deformation, created a highly
 1041 favorable synoptic-scale environment for sustained convection. These processes
 1042 supplied persistent forcing for ascent and low-level convergence, continuously
 1043 transporting moisture and instability to promote the organization and maintenance of
 1044 the circulation. By further examining the property of turbulent kinetic energy transfer

Formatted: Not Highlight

Deleted: the

Deleted: allowed for very

Deleted: very

Deleted: that

Deleted: ed

Deleted: T

Deleted: was enhanced by the evaporative cooling effect through the ...

Deleted: ¶

Deleted: , two convective segments subsequently merged into a well-organized squall system and moved perpendicular to the mean deep-layer wind/shear and developed a larger-scale bow-echo structure after reaching the plain.

Deleted: the RIJ behind the precipitation area by the superposition of ambient flow with the rotational flow on the west side of mesovortex. The calculation of the zonal momentum budget further confirmed the importance of the downward transport of horizontal momentum in accelerating lower-level flows in the descending RIJ.

Deleted: boundary layer

Deleted: the

Deleted: the

Deleted: provid

Deleted: which

Deleted: supplied

Deleted: , thereby

Deleted: ing

1072 derived from three-dimensional ultrasonic anemometers on the meteorological tower,
1073 we found that the frequency and intensity of inverse energy cascades increased
1074 significantly during this near-surface high wind event. These findings bridge the gap
1075 between meso- and small-scale physical processes in the lower troposphere and large-
1076 scale weather system, which potentially consolidate our understanding of the dynamics
1077 and their roles in the evolution of convection.

1078 Based on the above results, this case shares commonality with other QLCS cases
1079 in previous studies while exhibiting terrain-modulated uniqueness. Similar to QLCS
1080 events documented over plains (e.g., the U.S. Central Plains), the storm exhibited a
1081 well-defined cold pool, a descending RIJ, and strong low-level convergence leading to
1082 bow-echo development (Bentley and Mote, 1998; Bentley and Sparks, 2003; Wakimoto
1083 et al., 2006; Evans et al., 2014). However, its evolution was markedly influenced by
1084 complex topography (Houze, 2012). The initial convection was anchored and
1085 intensified by orographic lifting along the southern slopes of Mt. Yan, and the downhill
1086 propagation of the system resulted in an unusually concentrated zone of high
1087 reflectivity near the foot of Mt. Taihang. These findings underscore that while the
1088 overall dynamical framework of QLCS remains consistent, local topography can
1089 fundamentally alter the initiation, sustenance, and peak intensity of severe winds by
1090 modifying convergence patterns, cold-pool propagation, and vortex dynamics. Future
1091 nowcasting and high-resolution modeling for complex terrain regions should therefore
1092 explicitly incorporate such terrain-convection interactions.

1093 The novelty of this study lies in the utilization of high-resolution vertical
1094 observation derived from a rarely fine mesonet. These high-density multi-source
1095 observations enables us to explore the multiscale processes governing the generation of
1096 extreme gusty wind events. The mechanisms of convective evolution and its
1097 interactions with complex terrain in different stages have been elaborated, facilitating
1098 the characterization of such extreme wind events. More importantly, these findings
1099 underscore the value of RWP mesonet observations for advancing our understanding
1100 of extreme wind events and improving future nowcasting and prediction efforts.

- Deleted: ring
- Deleted: it was discovered
- Deleted: when
- Deleted: s occurred
- Deleted: the
- Deleted: ¶
- Deleted: has both
- Deleted: and terrain-modulated uniqueness
- Deleted: the
- Deleted: here
- Deleted: (Houze, 2012). Furthermore
- Deleted: Future forecasting in complex terrain regions should ... [6]
- Deleted: This study offers valuable insights into the ... [7]
- Deleted: Moreover,
- Deleted: these findings underscore the value of RWP ... [8]
- Deleted: T
- Deleted: at
- Deleted:
- Deleted: multiple observation with
- Deleted:
- Deleted: icit
- Deleted: explicit
- Deleted: an
- Deleted: using vertical observation with higher resolution ... [9]
- Deleted: RWPs provide valuable insights into capturing ... [10]
- Deleted: s
- Deleted: which are
- Deleted: vorable for
- Deleted: enhanc
- Deleted: in
- Deleted: the
- Deleted: in the future
- Deleted: These findings have important implications for ... [11]

1153 However, it should be mentioned that ~~the~~ RWPs have limited capability in detecting
1154 near-surface wind fields and thermal parameters. ~~Applying wind lidars and microwave~~
1155 radiometers ~~would help fill these~~ observational gaps and explore thermodynamic
1156 drivers of extreme winds.

Deleted: It's beneficial to

Deleted: a

Deleted: for

Deleted: ing

Deleted: ing

Formatted: Font: Times New Roman

1157 **Author contributions**

1158 JG designed the research framework and conceptualized this study; XG and JG
1159 conducted the experiment and drafted the initial manuscript; YS and FH helped the data
1160 collection from the meteorological tower and carried out data quality control; NL, ZZ,
1161 PY, SJ, LZ and TC participated in result interpretation and discussions; All authors
1162 contributed to the revision of the manuscript.

Formatted: Font: Times New Roman

1163 **Competing interests**

1164 The contact author has declared that there are no competing interests for all authors.

1165 **Financial support**

1166 This manuscript was supported by the National Natural Science Foundation of China
1167 under grant 42325501 and 42505015, Key Laboratory of South China Sea
1168 Meteorological Disaster Prevention and Mitigation of Hainan Province under grant
1169 SCSF202409, and the National Key Research and Development Program by the
1170 Ministry of Science and Technology in China under grant 2024YFC3013001.

1171 **Data availability**

1172 We are grateful to ECMWF for providing ERA5 hourly data by Copernicus Climate
1173 Change Service (C3S) Climate Data Store (CDS), which are available at
1174 <https://doi.org/10.24381/cds.bd0915c6> (Hersbach et al., 2023). The meteorological

Formatted: Font: Times New Roman

1180 measurements of automatic weather stations are obtained from the National
1181 Meteorological Information Center of China Meteorological Administration
1182 (<https://data.cma.cn>) via registration.

1183 References

- 1184 Abulikemu, A., Wang, Y., Gao, R., Wang, Y., and Xu, X.: A numerical study of
1185 convection initiation associated with a gust front in Bohai Bay Region, North
1186 China. *J. Geophys. Res. Atmos.*, 124, 13843 – 13860,
1187 <https://doi.org/10.1029/2019JD030883>, 2019.
- 1188 Adams-Selin, R. D., van den Heever, S. C., and Johnson, R. H.: Impact of Graupel
1189 parameterization schemes on idealized bow echo simulations. *Mon. Wea. Rev.*,
1190 141, 1241–1262, <https://doi.org/10.1175/MWR-D-12-00064.1>, 2013.
- 1191 Adler, B. and Kalthoff, N.: Multi-scale transport processes observed in the boundary
1192 layer over a mountainous island. *Bound.-Lay. Meteorol.*, 153, 515 – 537,
1193 <https://doi.org/10.1007/s10546-014-9957-8>, 2014.
- 1194 Atkins, N. T., Bouchard, C. S., Przybylinski, R. W., Trapp, R. J., and Schmocker, G.:
1195 Damaging surface wind mechanisms within the 10 June 2003 Saint Louis bow
1196 echo during BAMEX. *Mon. Wea. Rev.*, 133, 2275 – 2296,
1197 <https://doi.org/10.1175/MWR2973.1>, 2005).
- 1198 Atkins, N. T., and Laurent, M. St.: Bow echo mesovortices. Part I: Processes that
1199 influence their damaging potential. *Mon. Wea. Rev.*, 137, 1497 – 1513,
1200 <https://doi.org/10.1175/2008MWR2649.1>, 2009.
- 1201 Azorin-Molina, C., Guijarro, J.-A., Mcvicar, T. R., Vicente-Serrano, S. M., Chen, D.,
1202 Jerez, S., and Espirito-Santo, F.: Trends of daily peak wind gusts in Spain and
1203 Portugal, 1961–2014. *Journal of Geophysical Research: Atmospheres*, 121(3),
1204 1059–1078, <https://doi.org/10.1002/2015JD024485>, 2016.
- 1205 Barthelmie, R.J.: Evaluating the impact of wind induced roughness change and tidal
1206 range on extrapolation of offshore vertical wind speed profiles. *Wind Energ.*, 4:
1207 99-105, <https://doi.org/10.1002/we.45>, 2001.
- 1208 Beck, J., and Weiss, C.: An Assessment of Low-Level Baroclinity and Vorticity within
1209 a Simulated Supercell. *Mon. Wea. Rev.*, 141, 649 – 669,
1210 <https://doi.org/10.1175/MWR-D-11-00115.1>, 2013.

Deleted: &

Deleted: (

Deleted: 2019).

Formatted: Line spacing: single

Deleted: .

Formatted: Font: Times New Roman, 12 pt, Complex Script Font: 12 pt

Formatted: Font: Times New Roman, 12 pt, Complex Script Font: 12 pt

Deleted: &

Deleted: (

Deleted: 2013).

Deleted: .

Formatted (... [12])

Formatted: Font: 12 pt, Complex Script Font: 12 pt

Deleted: &

Deleted: (2014).

Deleted: .

Formatted (... [13])

Deleted: &

Moved down [6]: (2005).

Deleted: .

Deleted: (

Deleted: &

Deleted: (2009).

Deleted: .

Formatted (... [14])

Deleted: &

Deleted: (

Deleted: 2016).

Deleted: .

Formatted (... [15])

Formatted: Font: 12 pt, Complex Script Font: 12 pt

Formatted (... [16])

Deleted: (2001),

Deleted: .

Formatted: French

1235 Bélair, F., Dyer-Hawes, Q. and Romanic, D.: The Dynamics of the Urban Boundary
 1236 Layer Before and During a Severe Thunderstorm Outflow Over Downtown
 1237 Montreal, *Boundary-Layer Meteorol.*, 191, 6, [https://doi.org/10.1007/s10546-024-](https://doi.org/10.1007/s10546-024-00896-4)
 1238 [00896-4](https://doi.org/10.1007/s10546-024-00896-4), 2025.

1239 Bellamy, J. C.: Objective calculations of divergence, vertical velocity and vorticity.
 1240 *Bulletin of the American Meteorological Society*, 30(2), 45–49.
 1241 <https://doi.org/10.1175/1520-0477-30.2.45>, 1949.

1242 Bentley, M. L., and Sparks, J. M.: A 15 yr climatology of derecho-producing mesoscale
 1243 convective systems over the central and eastern United States. *Climate Res.*, 24,
 1244 129–139, 2003.

1245 Bentley, M. L., and Mote, T. L.: A Climatology of Derecho-Producing Mesoscale
 1246 Convective Systems in the Central and Eastern United States, 1986–95. Part I:
 1247 Temporal and Spatial Distribution. *Bull. Amer. Meteor. Soc.*, 79, 2527–2540,
 1248 [https://doi.org/10.1175/1520-0477\(1998\)079<2527:ACODPM>2.0.CO;2](https://doi.org/10.1175/1520-0477(1998)079<2527:ACODPM>2.0.CO;2), 1998.

1249 Bessho, K., Date, K., Hayashi, M., Ikeda, A., Imai, T., Inoue, H., et al.: An introduction
 1250 to Himawari-8/9—Japan's new-generation geostationary meteorological satellites.
 1251 *Journal of the Meteorological Society of Japan Series II*, 94(2), 151–183,
 1252 <https://doi.org/10.2151/jmsj.2016-009>, 2016

1253 Bluestein, H. B.: Fronts and Jet Streaks: A Theoretical Perspective. In P. S. Ray (Ed.),
 1254 *Mesoscale meteorology and forecasting* (pp. 173–215). American Meteorological
 1255 Society, https://doi.org/10.1007/978-1-935704-20-1_9, 1986.

1256 Bony, S., and Stevens, B.: Measuring area-averaged vertical motions with dropsondes.
 1257 *J. Atmos. Sci.*, 76, 767–783, <https://doi.org/10.1175/JAS-D-18-0141.1>, 2019.

1258 Bosart, L. R., and Sanders, F.: The Johnstown flood of July 1977: A long-lived
 1259 convective system. *J. Atmos. Sci.*, 38, 1616–1642, [https://doi.org/10.1175/1520-](https://doi.org/10.1175/1520-0469(1981)038<1616:TJFOJA>2.0.CO;2)
 1260 [0469\(1981\)038<1616:TJFOJA>2.0.CO;2](https://doi.org/10.1175/1520-0469(1981)038<1616:TJFOJA>2.0.CO;2), 1981.

1261 Burghardt, B. J., Evans, C., and Roebber, P. J.: Assessing the predictability of
 1262 convection initiation in the high plains using an object-based approach. *Weather*
 1263 *and Forecasting*, 29(2), 403–418, <https://doi.org/10.1175/WAF-D-13-00089.1>,
 1264 2014.

1265 Brandes, E. A., and Ziegler, C. L.: Mesoscale downdraft influences on vertical vorticity
 1266 in a mature mesoscale convective system. *Mon. Wea. Rev.*, 121, 1337–1353,
 1267 [https://doi.org/10.1175/1520-0493\(1993\)121<1337:MDIOVV>2.0.CO;2](https://doi.org/10.1175/1520-0493(1993)121<1337:MDIOVV>2.0.CO;2), 1993.

1268 Broward, F.K., and Winant, C.D.: Laboratory observations of shear-layer instability in
 1269 a stratified fluid. *Boundary-Layer Meteorol.*, 5: 67–77,
 1270 <https://doi.org/10.1007/BF02188312>, 1973.

1271 Browning, K.A., Marsham, J.H., Nicol, J.C., Perry, F.M., White, B.A., Blyth, A.M. and

Deleted: &...nd Romanic, D. (2025). (... [17])

Formatted: French

Deleted: Montréal

Deleted: .

Formatted: Hyperlink, Font: DengXian, 10.5 pt, Complex Script Font: 11 pt

Deleted: (1949).....Objective calculations of divergence, vertical velocity and vorticity. *Bulletin of the American Meteorological Society*, 30(2), 45–49. (... [18])

Formatted (... [19])

Deleted: &...nd Sparks, J. M. (2003).... A 15 yr...5 yr climatology of derecho-producing mesoscale convective systems over the central and eastern United States. *Climate Res.*, 24, 129 — (... [20])

Deleted: &...nd Mote, T. L. (1998).... A Climatology of Derecho-Producing Mesoscale Convective Systems in the Central and Eastern United States, 1986–95. Part I: Temporal and Spatial Distribution. *Bull. Amer. Meteor. Soc.*, 79, 2527–2540. (... [21])

Formatted (... [22])

Deleted: (2016).... An introduction to Himawari-8/9—Japan's new-generation geostationary meteorological satellites. *Journal of the Meteorological Society of Japan Series II*, 94(2), 151–183. (... [23])

Formatted: Hyperlink, Font: DengXian, 10.5 pt, Complex Script Font: 11 pt

Deleted: (1986)....Fronts and Jet Streaks: A Theoretical Perspective. In P. S. Ray (Ed.), *Mesoscale meteorology and forecasting* (pp. 173–215). American Meteorological Society. (... [24])

Formatted: Hyperlink, Font: DengXian, 10.5 pt, Complex Script Font: 11 pt

Deleted: &...nd Stevens, B.: (2019)....Measuring area-averaged vertical motions with dropsondes. *J. Atmos. Sci.*, 76, 767–783. (... [25])

Formatted (... [26])

Deleted: &...nd Sanders, F.: (1981). (... [27])

Deleted: &...nd Roebber, P. J., (2014)....Assessing the (... [28])

Formatted (... [29])

Deleted: &...nd Ziegler, C. L.: (1993)....Mesoscale (... [30])

Formatted: Hyperlink, Font: DengXian, 10.5 pt, Complex Script Font: 11 pt

1361 Mobbs, S.D.: Observations of dual slantwise circulations above a cool
1362 undercurrent in a mesoscale convective system. Q.J.R. Meteorol. Soc., 136: 354-
1363 373, <https://doi.org/10.1002/qj.582>, 2010.

1364 Byrne, D., and Zhang, J. A.: Height-dependent transition from 3-D to 2-D turbulence
1365 in the hurricane boundary layer. Geophysical Research Letters, 40(7), 1439–1442,
1366 <https://doi.org/10.1002/grl.50335>, 2013.

1367 Chen, D., Guo, J., Yao, D., Lin, Y., Zhao, C., Min, M., et al.: Mesoscale convective
1368 systems in the Asian monsoon region from Advanced Himawari Imager:
1369 Algorithms and preliminary results. Journal of Geophysical Research:
1370 Atmospheres, 124, 2210–2234, <https://doi.org/10.1029/2018JD029707>, 2019.

1371 Chen, M., Wang, Y., Gao, F., and Xiao, X.: Diurnal variations in convective storm
1372 activity over contiguous North China during the warm season based on radar
1373 mosaic climatology. J. Geophys. Res.-Atmos., 117, D20115,
1374 <https://doi.org/10.1029/2012JD018158>, 2012.

1375 Chen, M., Wang, Y., Gao, F., and Xiao, X.: Diurnal evolution and distribution of warm
1376 - season convective storms in different prevailing wind regimes over contiguous
1377 North China. J. Geophys. Res.-Atmos., 119, 2742–2763, 2014.

1378 Chen, T., Guo, J., Guo, X., Zhang, Y., Xu, H., and Zhang, D.-L.: On the multiscale
1379 processes leading to an extreme gust wind event in East China: Insights from radar
1380 wind profiler mesonet observations. Journal of Geophysical Research:
1381 Atmospheres, 129, e2024JD041484, <https://doi.org/10.1029/2024JD041484>,
1382 2024.

1383 Coniglio, M. C., Corfidi, S. F., and Kain, J. S.: Environment and early evolution of the
1384 8 May 2009 derecho-producing convective system. Mon. Wea. Rev., 139, 1083–
1385 1102, <https://doi.org/10.1175/2010MWR3413.1>, 2011.

1386 Da, C.: Preliminary assessment of the Advanced Himawari Imager (AHI) measurement
1387 onboard Himawari-8 geostationary satellite. Remote Sensing Letters, 6, 637–646,
1388 <https://doi.org/10.1080/2150704x.2015.1066522>, 2015.

1389 Dai, C., Wang, Q., Kalogiros, J. A., Lenschow, D. H., Gao, Z., and Zhou, M.:
1390 Determining boundary-layer height from aircraft measurements. Bound.-Lay.
1391 Meteorol., 152, 277–302, <https://doi.org/10.1007/s10546-014-9929-z>, 2014.

1392 Davis, C. A., and Trier, S. B.: Mesoscale convective vortices observed during BAMEX.
1393 Part I: Kinematic and thermodynamic structure. Monthly Weather Review, 135(6),
1394 2029–2049, <https://doi.org/10.1175/MWR3398.1>, 2007.

1395 Dodson, D. S. and Small Griswold, J. D.: Turbulent and boundary layer characteristics
1396 during VOCALS-REx. Atmos. Chem. Phys., 21, 1937–1961,
1397 <https://doi.org/10.5194/acp-21-1937-2021>, 2021.

1398 Emanuel, K. A.: Frontal Circulations in the Presence of Small Moist Symmetric
1399 Stability. J. Atmos. Sci., 42, 1062–1071, [https://doi.org/10.1175/1520-0469\(1985\)042<1062:FCITPO>2.0.CO;2](https://doi.org/10.1175/1520-0469(1985)042<1062:FCITPO>2.0.CO;2), 1985.

1400 Evans, C., Weisman, M. L., and Bosart, L. F.: Development of an intense, warm-core
1401 mesoscale vortex associated with the 8 May 2009 “super derecho” convective
1402 event. J. Atmos. Sci., 71, 1218–1240, <https://doi.org/10.1175/JAS-D-13-0167.1>,
1403

Formatted: Hyperlink, Font: DengXian, 10.5 pt, Complex Script Font: 11 pt

Deleted: &...nd Zhang, J. A.: (2013)...Height-dependent transition from 3-D to 2-D turbulence in the hurricane boundary layer. Geophysical Research Letters, 40(7), 1439–1442. (... [31])

Formatted (... [32])

Deleted: (2019)...Mesoscale convective systems in the Asian monsoon region from Advanced Himawari Imager: Algorithms and preliminary results. Journal of Geophysical Research: Atmospheres, 124, 2210–2234. (... [33])

Field Code Changed

Deleted: &...nd Xiao, X.: (2012). (... [34])

Deleted: &...nd Xiao, X.: (2014). (... [35])

Deleted: &...nd Zhang, D.-L.: (2024)...On the multiscale processes leading to an extreme gust wind event in East China: Insights from radar wind profiler mesonet observations. Journal of Geophysical Research: Atmospheres, 129, e2024JD041484. (... [36])

Formatted (... [37])

Deleted: &...nd Kain, J. S.: (2011)...Environment and early evolution of the 8 May 2009 derecho-producing convective system. Mon. Wea. Rev., 139, 1083–1102 (... [38])

Formatted (... [39])

Deleted: (2015)...Preliminary assessment of the Advanced Himawari Imager (AHI) measurement onboard Himawari-8 geostationary satellite. Remote Sensing Letters, 6, 637–646. (... [40])

Deleted: &...nd Zhou, M.: (2014)...Determining boundary-layer height from aircraft measurements. Bound.-Lay (... [41])

Field Code Changed

Deleted: &...nd Trier, S. B.: (2007)...Mesoscale convective vortices observed during BAMEX. Part I (... [42])

Formatted (... [43])

Deleted: &...nd Small Griswold, J. D.: (2021)...Turbulent and boundary layer characteristics during VOCALS-REx (... [44])

Deleted: (1985)...Frontal Circulations in the Presence of Small Moist Symmetric Stability. J. Atmos. Sci., 42, 1062–1071 (... [45])

Deleted: &...nd Bosart, L. F.: (2014)...Development of an intense, warm-core mesoscale vortex associated with the 8 May 2009 “super derecho” convective event. J. Atmos. Sci., 71, 1218–1240 (... [46])

Formatted (... [47])

1511 2014.

1512 Fiori, E., Parodi, A., and Siccardi, F.; Uncertainty in prediction of deep moist
 1513 convective processes: Turbulence parameterizations, microphysics and grid-scale
 1514 effects. *Atmospheric Research*, 100(4), 447 – 456.
 1515 <https://doi.org/10.1016/j.atmosres.2010.10.003>, 2011.

1516 Fovell, R. G.; Upstream influence of numerically simulated squall-line storms. *Quart.*
 1517 *J. Roy. Meteor. Soc.*, 128, 893–912. <https://doi.org/10.1256/0035900021643737>,
 1518 2002.

1519 Fovell, R. G., and Cao, Y.; Wind and gust forecasting in complex terrain. 15th WRF
 1520 Users Workshop, Boulder, CO, NCAR,
 1521 5A.2, <http://www2.mmm.ucar.edu/wrf/users/workshops/WS2014/ppts/5A.2.pdf>,
 1522 2014.

1523 French, A. J., and Parker, M. D.; Observations of mergers between squall lines and
 1524 isolated supercell thunderstorms. *Wea. Forecasting*, 27, 255 – 278.
 1525 <https://doi.org/10.1175/WAF-D-11-00058.1>, 2012.

1526 French, A. J., and Parker, M. D.; Numerical simulations of bow echo formation
 1527 following a squall line–supercell merger. *Mon. Wea. Rev.*, 142, 4791–4822.
 1528 <https://doi.org/10.1175/MWR-D-13-00356.1>, 2014.

1529 Fujita, T. T.; Manual of downburst identification for Project NIMROD. *Satellite and*
 1530 *Mesometeorology Research Paper* 156, 111 pp.,
 1531 <https://ntrs.nasa.gov/citations/19780022828>, 1978.

1532 Goyette, S., Brasseur, O., and Beniston, M.; Application of a new wind gust
 1533 parameterization: Multiscale case studies performed with the Canadian regional
 1534 climate model. *Journal of Geophysical Research: Atmospheres*, 108, 4374.
 1535 doi:10.1029/2002JD002646, D13, 2003.

1536 Guo, J., Liu, B., Gong, W., Shi, L., Zhang, Y., Ma, Y., Zhang, J., Chen, T., Bai, K.,
 1537 Stoffelen, A., de Leeuw, G., and Xu, X.; Technical note: First comparison of wind
 1538 observations from ESA's satellite mission Aeolus and ground-based radar wind
 1539 profiler network of China. *Atmos. Chem. Phys.*, 21, 2945–2958,
 1540 <https://doi.org/10.5194/acp-21-2945-2021>, 2021a.

1541 Guo, J., Zhang, J., Yang, K., Liao, H., Zhang, S., Huang, K., Lv, Y., Shao, J., Yu, T.,
 1542 Tong, B., Li, J., Su, T., Yim, S. H. L., Stoffelen, A., Zhai, P., and Xu, X.;
 1543 Investigation of near-global daytime boundary layer height using high-resolution
 1544 radiosondes: First results and comparison with ERA-5, MERRA-2, JRA-55, and
 1545 NCEP-2 reanalyses. *Atmos. Chem. Phys.*, 21, 17079 – 17097.
 1546 <https://doi.org/10.5194/acp-21-17079-2021>, 2021b.

1547 Guo, X., Guo, J., Zhang, D-L., and Yun, Y.; Vertical divergence profiles as detected by
 1548 two wind profiler mesonets over East China: implications for nowcasting

Deleted: &...nd Siccardi, F.: (2011)...Uncertainty in prediction of deep moist convective processes: Turbulence parameterizations, microphysics and grid-scale effects. *Atmospheric Research*, 100(4), 447–456. (... [48])

Formatted (... [49])

Deleted: ... (2002)...Upstream influence of numerically simulated squall-line storms. *Quart. J. Roy. Meteor. Soc.*, 128, 893–912. (... [50])

Formatted (... [51])

Deleted: Cao, (2014).

Formatted (... [52])

Deleted: &...nd Parker, M. D. (2012)... Observations of mergers between squall lines and isolated supercell thunderstorms. *Wea. Forecasting*, 27, 255–278. (... [53])

Formatted (... [54])

Deleted: &...nd Parker, M. D. (2014)... Numerical simulations of bow echo formation following a squall line–supercell merger. *Mon. Wea. Rev.*, 142, 4791–4822. (... [55])

Formatted: Hyperlink, Font: DengXian, 10.5 pt, Complex Script Font: 11 pt

Deleted: (1978)... Manual of downburst identification for Project NIMROD. *Satellite and Mesometeorology Research Paper* 156, 111 pp., . (... [56])

Formatted: Hyperlink, Font: DengXian, 10.5 pt, Complex Script Font: 11 pt

Deleted: &...nd Beniston, M. (2003)... Application of a new wind gust parameterization: Multiscale case studies performed with the Canadian regional climate model. *Journal of Geophysical Research: Atmospheres*, 108, 4374. (... [57])

Formatted (... [58])

Deleted: (2021a).

Formatted (... [59])

Formatted (... [60])

Field Code Changed

Deleted: &...nd Xu, X. (2021b)... Investigation of near-global daytime boundary layer height using high-resolution radiosondes: First results and comparison with ERA-5, MERRA-2, JRA-55, and NCEP-2 reanalyses. *Atmos. Chem. Phys.*, 21, 17079–17097. (... [61])

Deleted: ¶

Deleted: &...nd Yun, Y. (2023). (... [62])

1620 convective storms, Q. J. R. Meteorol. Soc., 149(754), 1629-1649,
 1621 doi:10.1002/qj.4474, 2023.

1622 Guo, X., Guo, J., Chen, T., Li, N., Zhang, F., and Sun, Y.: Revisiting the evolution of
 1623 downhill thunderstorms over Beijing: a new perspective from a radar wind profiler
 1624 mesonet, Atmos. Chem. Phys., 24, 8067–8083, [https://doi.org/10.5194/acp-24-](https://doi.org/10.5194/acp-24-8067-2024)
 1625 [8067-2024](https://doi.org/10.5194/acp-24-8067-2024), 2024.

1626 Guzman-Morales, J., Gershunov, A., Theiss, J., Li, H., and Cayan, D.: Santa Ana Winds
 1627 of Southern California: Their climatology, extremes, and behavior spanning six
 1628 and a half decades, Geophys. Res. Lett., 43, 2827 – 2834,
 1629 <https://doi.org/10.1002/2016GL067887>, 2016.

1630 Grim, J. A., Rauber, R. M., McFarquhar, G. M., Jewett, B. F., and Jorgensen, D. P.:
 1631 Development and forcing of the rear inflow jet in a rapidly developing and
 1632 decaying squall line during BAMEX. Monthly Weather Review, 137(4), 1206–
 1633 1229, <https://doi.org/10.1175/2008mwr2503.1>, 2009.

1634 Grubišić, V., Doyle, J. D., Kuettner, J., Mobbs, S., Smith, R. B., Whiteman, C. D., Dirks,
 1635 R., Czyzyk, S., Cohn, S. A., Vosper, S., Weissmann, M., Haimov, S., De Wekker,
 1636 S. F. J., Pan, L. L., and Chow, F. K.: The terrain-induced rotor experiment: A field
 1637 campaign overview including observational highlights. Bulletin of the American
 1638 Meteorological Society, 89, 1513–1534, <https://doi.org/10.1175/2008BAMS2487.1>,
 1639 2008.

1640 Hadavi, M., and Romanic, D.: Atmospheric conditions conducive to thunderstorms
 1641 with downbursts in Canada and a downburst precursor parameter. Atmos. Res.,
 1642 305(107), 428, <https://doi.org/10.1016/j.atmosres.2024.107428>, 2024.

1643 Han, B., Du, Y., Wu, C., and Liu, X.: Microphysical characteristics of the coexisting
 1644 frontal and warm-sector heavy rainfall in South China. Journal of Geophysical
 1645 Research: Atmospheres, 126, e2021JD035446,
 1646 <https://doi.org/10.1029/2021JD035446>, 2021.

1647 Haerter, J. O., Böing, S. J., Henneberg, O., and Nissen, S. B.: Circling in on convective
 1648 organization. Geophysical Research Letters, 46(12), 7024 – 7034,
 1649 <https://doi.org/10.1029/2019GL082092>, 2019.

1650 Harris, A. R., and Kahl, J. D. W.: Gust factors: Meteorologically stratified climatology,
 1651 data artifacts, and utility in forecasting peak gusts. Journal of Applied
 1652 Meteorology and Climatology, 56(12), 3151–3166, [https://doi.org/10.1175/jamc-](https://doi.org/10.1175/jamc-d-17-0133.1)
 1653 [d-17-0133.1](https://doi.org/10.1175/jamc-d-17-0133.1), 2017.

1654 Hirt, M., and Craig, G. C.: A cold pool perturbation scheme to improve convective
 1655 initiation in convection-permitting models. Quarterly Journal of the Royal
 1656 Meteorological Society, 147(737), 2429–2447, <https://doi.org/10.1002/qj.4032>,

- Deleted: .
- Deleted: &...nd Sun, Y. (2024)... Revisiting the evolution of downhill thunderstorms over Beijing: a new perspective from a radar wind profiler mesonet, Atmos. Chem. Phys., 24, 8067–8083. (... [63])
- Formatted (... [64])
- Deleted: Gershunov... Theiss, J. Theiss... Li, H. Li... and Cayan, D. Cayan (2016), (... [65])
- Formatted: Hyperlink, Font: DengXian, 10.5 pt, Complex Script Font: 11 pt
- Deleted: &...nd Jorgensen, D. P. (2009)... Development and forcing of the rear inflow jet in a rapidly developing and decaying squall line during BAMEX. Monthly Weather Review, 137(4), 1206–1229. (... [66])
- Formatted (... [67])
- Formatted (... [68])
- Formatted: Line spacing: single
- Deleted: Grubišić, Vanda and Doyle, James D. and Kuettner, Joachim and Mobbs, Stephen and Smith, Ronald B. and Whiteman, C. David and Dirks, Richard and Czyzyk, Stanley and Cohn, Stephen A. and Vosper, Simon and Weissmann, Martin and Haimov, Samuel and De Wekker, Stephan F.J. and Pan, Laura L. and Chow, Fotini Katopodes (2008) The terrain-induced rotor experiment: A field campaign overview including observational highlights. Bulletin of the American Meteorological Society, pp. 1-21. American Meteorological Society. doi: 10.1175/2008BAMS2487.1. (... [69])
- Formatted: Hyperlink, Font: DengXian, 10.5 pt, Complex Script Font: 11 pt
- Deleted: &...nd Liu, X. (2021)... Microphysical characteristics of the coexisting frontal and warm-sector heavy rainfall in South China. Journal of Geophysical Research: Atmospheres, 126, e2021JD035446. (... [70])
- Formatted: Swedish
- Formatted (... [71])
- Formatted: Hyperlink, Font: DengXian, 10.5 pt, Complex Script Font: 11 pt
- Deleted: &...nd Kahl, J. D. W. (2017)... Gust factors: Meteorologically stratified climatology, data artifacts (... [72])
- Field Code Changed
- Deleted: (... [73])
- Formatted (... [74])

1732 2021.

1733 Houze, R. A. Jr.: Orographic effects on precipitating clouds, *Rev. Geophys.*, 50,

1734 RG1001, doi:10.1029/2011RG000365, 2012.

1735 Houze, R. A. Jr.: Chapter 9—Mesoscale convective systems. In R. A. Houze, Jr. (Ed.),

1736 *International geophysics* (pp. 237 – 286). Academic Press.

1737 <https://doi.org/10.1016/B978-0-12-374266-7.00009-3>, 2014.

1738 [Houze, R. A., Rutledge, S. A., Biggerstaff, M. I., and Smull, B. F.; Interpretation of](#)

1739 [Doppler Weather Radar Displays of Midlatitude Mesoscale Convective](#)

1740 [Systems. *Bull. Amer. Meteor. Soc.*, 70, 608–619, \[https://doi.org/10.1175/1520-\]\(https://doi.org/10.1175/1520-0477\(1989\)070<0608:IODWRD>2.0.CO;2\)](#)

1741 [0477\(1989\)070<0608:IODWRD>2.0.CO;2, 1989.](#)

1742 Johns, R. H., and Hirt, W. D.; Derechos: Widespread convectively induced windstorms.

1743 *Wea. Forecasting*, 2, 32–49, [https://doi.org/10.1175/1520-](https://doi.org/10.1175/1520-0434(1987)002<0032:DWCIW>2.0.CO;2)

1744 [0434\(1987\)002<0032:DWCIW>2.0.CO;2, 1987.](#)

1745 Kahl, J. D. W.; Forecasting peak wind gusts using meteorologically stratified gust

1746 factors and MOS guidance. *Weather and Forecasting*, 35(3), 1129–1143,

1747 <https://doi.org/10.1175/waf-d-20-0045.1>, 2020.

1748 Kelley, D. I., Burton, C., Di Giuseppe, F., Jones, M. W., Barbosa, M. L. F., Brambleby,

1749 E., McNorton, J. R., Liu, Z., Bradley, A. S. I., Blackford, K., Burke, E., Ciavarella,

1750 A., Di Tomaso, E., Eden, J., Ferreira, I. J. M., Fiedler, L., Hartley, A. J., Keeping,

1751 T. R., Lampe, S., Lombardi, A., Mataveli, G., Qu, Y., Silva, P. S., Spuler, F. R.,

1752 Steinmann, C. B., Torres-Vázquez, M. Á., Veiga, R., van Wees, D., Wessel, J. B.,

1753 Wright, E., Bilbao, B., Bourbonnais, M., Gao, C., Di Bella, C. M., Dintwe, K.,

1754 Donovan, V. M., Harris, S., Kukavskaya, E. A., N'Dri, A. B., Santín, C., Selaya,

1755 G., Sjöström, J., Abatzoglou, J. T., Andela, N., Carmenta, R., Chuvieco, E., Giglio,

1756 L., Hamilton, D. S., Hantson, S., Meier, S., Parrington, M., Sadegh, M., San-

1757 Miguel-Ayanz, J., Sedano, F., Turco, M., van der Werf, G. R., Veraverbeke, S.,

1758 Anderson, L. O., Clarke, H., Fernandes, P. M., and Kolden, C. A.: State of

1759 Wildfires 2024 – 2025, *Earth Syst. Sci. Data*, 17, 5377 – 5488,

1760 <https://doi.org/10.5194/essd-17-5377-2025>, 2025.

1761 Kolmogorov, A. N.; The local structure of turbulence in incompressible viscous fluid

1762 for very large Reynolds numbers. *Doklady Akademii Nauk SSSR*, 30, 299–303,

1763 1941.

1764 Kraichnan, R. H.; Inertial ranges in two-dimensional turbulence. *The Physics of Fluids*,

1765 10(7), 1417–1423, <https://doi.org/10.1063/1.1762301>, 1967.

1766 Lafore, J., and Moncrieff, M. W.; A numerical investigation of the organization and

1767 interaction of the convective and stratiform regions of tropical squall lines. *Journal*

1768 *of the Atmospheric Sciences*, 46(4), 521–544. [https://doi.org/10.1175/1520-](https://doi.org/10.1175/1520-0469(1989)046<0521:ANIOTO>2.0.CO;2)

1769 [0469\(1989\)046<0521:ANIOTO>2.0.CO;2, 1989.](#)

1770 Lenschow, D. H., Savic-Jovicic, V., and Stevens, B.; Divergence and vorticity from

1771 aircraft air motion measurements. *J. Atmos. Oceanic Technol.*, 24, 2062–2072,

1772 <https://doi.org/10.1175/2007JTECHA940.1>, 2007

Formatted: Font: Times New Roman, 12 pt, Complex Script Font: 12 pt

Deleted: Rutledge

Deleted: Biggerstaff

Deleted: Smull

Formatted: Font: Not Italic, Complex Script Font: Not Italic

Formatted: Font: Not Bold, Complex Script Font: Not Bold

Formatted: Default Paragraph Font, Font: DengXian, 10.5 pt, Complex Script Font: 11 pt

Deleted: &

Deleted: (1987).

Formatted: Font: (Asian) DengXian

Deleted: .

Formatted: Font: Times New Roman, 12 pt, Complex Script Font: 12 pt

Formatted: Font: 12 pt, Complex Script Font: 12 pt

Formatted: Font: (Asian) +Body Asian (SimSun)

Deleted: (2020).

Deleted: .

Formatted: Font: Times New Roman, 12 pt, Complex Script Font: 12 pt

Formatted: Font: 12 pt, Complex Script Font: 12 pt

Deleted: (1941).

Deleted: (1967).

Deleted: .

Formatted: Font: Times New Roman, 12 pt, Complex Script Font: 12 pt

Formatted: Font: 12 pt, Complex Script Font: 12 pt

Formatted: Font: (Asian) +Body Asian (SimSun)

Deleted: &

Deleted: (1989).

Formatted: Font: Times New Roman, 12 pt, Complex Script Font: 12 pt

Formatted: Font: 12 pt, Complex Script Font: 12 pt

Formatted: Font: (Asian) +Body Asian (SimSun)

Deleted: &

Deleted: (2007).

Formatted: Font: Times New Roman, 12 pt, Complex Script Font: 12 pt

Formatted: Font: 12 pt, Complex Script Font: 12 pt

1788 Letson, F., Pryor, S. C., Barthelmie, R. J., and Hu, W.: Observed gust wind speeds in
1789 the coterminous United States, and their relationship to local and regional
1790 drivers. *J. Wind Eng. Ind. Aerodyn.*, 173, 199–
1791 209, <https://doi.org/10.1016/j.jweia.2017.12.008>, 2018.

1792 Li, H., Cui, X., and Zhang, D. L.: On the initiation of an isolated heavy-rain-producing
1793 storm near the central urban area of Beijing metropolitan region, *Mon. Weather*
1794 *Rev.*, 145, 181–197, <https://doi.org/10.1175/MWR-D-16-0115.1>, 2017.

1795 Liu, B., Guo, J., Gong, W., Shi, L., Zhang, Y., and Ma, Y.: Characteristics and
1796 performance of wind profiles as observed by the radar wind profiler network of
1797 China. *Atmospheric Measurement Techniques*, 13(8), 4589–4600,
1798 <https://doi.org/10.5194/amt-13-4589-2020>, 2020.

1799 Liu, B., Ma, X., Guo, J., Wen, R., Li, H., Jin, S., Ma, Y., Guo, X., and Gong, W.:
1800 [Extending the wind profile beyond the surface layer by combining physical and
1801 machine learning approaches](https://doi.org/10.5194/acp-24-4047-2024), *Atmos. Chem. Phys.*, 24, 4047–4063,
1802 <https://doi.org/10.5194/acp-24-4047-2024>, 2024.

1803 Liu, Q., Xu, X., Zhao, K., and Zhou, A.: A merger-formation bow echo caused by low-
1804 level mesovortex in South China. *Journal of Geophysical Research: Atmospheres*,
1805 128, e2022JD037954, <https://doi.org/10.1029/2022JD037954>, 2023.

1806 Lombardo, K., and Kumjian, M. R.: Observations of the Discrete Propagation of a
1807 Mesoscale Convective System during RELAMPAGO – CACTI. *Mon. Wea. Rev.*,
1808 150, 2111 – 2138, <https://doi.org/10.1175/MWR-D-21-0265.1>, 2022.

1809 Luchetti, N. T., Friedrich, K., Rodell, C. E., and Lundquist, J. K.: Characterizing
1810 thunderstorm gust fronts near complex terrain. *Monthly Weather Review*, 148(8),
1811 3267–3286, <https://doi.org/10.1175/mwr-d-19-0316.1>, 2020.

1812 Luu, L. N., van Meijgaard, E., Philip, S. Y., Kew, S. F., de Baar, J. H. S., and Stepek,
1813 A.: Impact of surface roughness changes on surface wind speed over western
1814 Europe: A study with the regional climate model RACMO. *Journal of Geophysical*
1815 *Research: Atmospheres*, 128, e2022JD038426,
1816 <https://doi.org/10.1029/2022JD038426>, 2023.

1817 Lyu, M., Potter, H., Collins, C. O., Yang, X., and Wang, X.: The impacts of gustiness
1818 on the evolution of surface gravity waves. *Geophysical Research Letters*, 50(12),
1819 <https://doi.org/10.1029/2023gl104085>, 2023.

1820 Mahoney, K. M., and Lackmann, G. M.: The sensitivity of momentum transport and
1821 severe surface winds to environmental moisture in idealized simulations of a
1822 mesoscale convective system. *Monthly Weather Review*, 139(5), 1352–1369,
1823 <https://doi.org/10.1175/2010mwr3468.1>, 2011.

1824 Mahoney, K. M., Lackmann, G. M., and Parker, M. D.: The role of momentum
1825 transport in the motion of a quasi-idealized mesoscale convective system. *Monthly*
1826 *Weather Review*, 137(10), 3316–3338, <https://doi.org/10.1175/2009mwr2895.1>,
1827 2009.

1828 Mahrt, L., Vickers, D., Frederickson, P., Davidson, K., and Smedman, A.-S.: Sea-
1829 surface aerodynamic roughness. *J. Geophys. Res.*, 108, 3171,
1830 [doi:10.1029/2002JC001383](https://doi.org/10.1029/2002JC001383), C6, 2003

Deleted: Pryor... Barthelmie ... R. J. Barthelmie... and Hu, W. Hu (2018). (... [75])

Formatted: Swedish (... [76])

Formatted (... [76])

Deleted: &...nd Zhang, D. L. (2017)... On the initiation of an isolated heavy-rain-producing storm near the central urban area of Beijing metropolitan region, *Mon. Weather Rev.*, 145, 181–197. (... [77])

Formatted: Italian (... [77])

Formatted (... [78])

Deleted: &...nd Ma, Y. (2020)... Characteristics and performance of wind profiles as observed by the radar wind profiler network of China. *Atmospheric Measurement Techniques*, 13(8), 4589–4600. (... [79])

Formatted (... [80])

Deleted: (2024).

Formatted: Font: (Default) Times New Roman, (Asian) Times New Roman, 12 pt, Complex Script Font: 12 pt

Formatted (... [81])

Formatted (... [82])

Formatted: Indent: Before: 0 cm, Hanging: 2 ch, Line spacing: single

Formatted: Line spacing: single

Deleted: &...nd Zhou, A. (2023)... A merger-formation bow echo caused by low-level mesovortex in South China. *Journal of Geophysical Research: Atmospheres*, 128, e2022JD037954. (... [83])

Formatted (... [84])

Formatted: Hyperlink, Font: (Default) DengXian, (Asian) DengXian, 10.5 pt, Complex Script Font: 11 pt

Deleted: &...nd Lundquist, J. K. (2020)... Character... (... [85])

Formatted (... [86])

Deleted: ¶

Deleted: &...nd Stepek, A. (2023)... Impact of surf... (... [87])

Formatted: Dutch (... [87])

Formatted (... [88])

Deleted: &...nd Wang, X. (2023)... The impacts of (... [89])

Formatted (... [90])

Deleted: &...nd Lackmann, G. M. (2011)... The (... [91])

Formatted (... [92])

Deleted: &...nd Parker, M. D. (2009)... The role of (... [93])

Formatted (... [94])

1927	Marino, R., Pouquet, A., and Rosenberg, D.: Resolving the paradox of oceanic large-scale balance and small-scale mixing. <i>Physical Review Letters</i> , 114(11), 114504. https://doi.org/10.1103/physrevlett.114.114504 , 2015.	Deleted: &...nd Rosenberg, D. ... (2015)... Resolving the paradox of oceanic large-scale balance and small-scale mixing. <i>Physical Review Letters</i> , 114(11), 114504. ... [95]
1928		
1929		
1930	Meng, Z., Zhang, F., Markowski, P., Wu, D., and Zhao, K.: A modeling study on the development of a bowing structure and associated rear inflow within a squall line over South China. <i>J. Atmos. Sci.</i> , 69, 1182–1207, https://doi.org/10.1175/JAS-D-11-0121.1 , 2012.	Deleted:
1931		
1932		Deleted: &...nd Zhao, K. (2012). ... [96]
1933		Formatted ... [97]
1934	Miller, J. E.: ON THE CONCEPT OF FRONTOGENESIS. <i>J. Atmos. Sci.</i> , 5, 169–171. <a href="https://doi.org/10.1175/1520-0469(1948)005<0169:OTCOF>2.0.CO;2">https://doi.org/10.1175/1520-0469(1948)005<0169:OTCOF>2.0.CO;2 , 1948.	Deleted: (1948)... ON THE CONCEPT OF FRONTOGENESIS. <i>J. Atmos. Sci.</i> , 5, 169–171. ... [98]
1935		
1936	Monahan, A. H., Rees, T., He, Y., and McFarlane, N.: Multiple regimes of wind, stratification, and turbulence in the stable boundary layer. <i>Journal of the Atmospheric Sciences</i> , 72(8), 3178–3198. https://doi.org/10.1175/jas-d-14-0311.1 , 2015.	Formatted ... [99]
1937		
1938		Deleted: &...nd McFarlane, N. (2015)... Multiple regimes of wind, stratification, and turbulence in the stable boundary layer. <i>Journal of the Atmospheric Sciences</i> , 72(8), 3178–3198. ... [100]
1939		
1940	Monin, A. S., and Obukhov, A. M.: Basic laws of turbulent mixing in the surface layer of the atmosphere. <i>Tr. Akad. Nauk SSSR Geophys. Inst.</i> , 24, 163, 1954.	Deleted: &...nd Obukhov, A. M. (1954). ... [101]
1941		
1942	Neiman, P. J., Hardesty, R. M., Shapiro, M. A., and Cupp, R. E.: Doppler Lidar Observations of a Downslope Windstorm. <i>Mon. Wea. Rev.</i> , 116, 2265–2275. <a href="https://doi.org/10.1175/1520-0493(1988)116<2265:DLOAD>2.0.CO;2">https://doi.org/10.1175/1520-0493(1988)116<2265:DLOAD>2.0.CO;2 , 1988.	Formatted: Hyperlink, Font: (Default) DengXian, (Asian) DengXian, 10.5 pt, Complex Script Font: 11 pt
1943		
1944		
1945	Nitta, T., and Esbensen, S.: Heat and moisture budget analyses using BOMEX data. <i>Mon. Wea. Rev.</i> , 102, 17–28. https://doi.org/10.1175/1520-0493(1974)102.0017:HAMBAU.2.0.CO;2 , 1974.	Deleted: &...nd Esbensen, S. (1974)... Heat and moisture budget analyses using BOMEX data. <i>Mon. Wea. Rev.</i> , 102, 17–28. ... [102]
1946		
1947		
1948	Oke, T.: <i>Boundary Layer Climates</i> . Academic Press, 345 pp, 1987.	Formatted ... [103]
1949	Pandya, R. E., and Durran, D. R.: The influence of convectively generated thermal forcing on the mesoscale circulation around squall lines. <i>J. Atmos. Sci.</i> , 53, 2924–2951. <a href="https://doi.org/10.1175/1520-0469(1996)053<2924:TIOCGT>2.0.CO;2">https://doi.org/10.1175/1520-0469(1996)053<2924:TIOCGT>2.0.CO;2 , 1996.	Deleted: ¶ ... [104]
1950		
1951		Deleted: &...nd Durran, D. R. (1996)... The influence of convectively generated thermal forcing on the mesoscale circulation around squall lines. <i>J. Atmos. Sci.</i> , 53, 2924–2951. ... [105]
1952		
1953	Peterson, T. C., Karl, T. R., Kossin, J. P., Kunkel, K. E., Lawrimore, J. H., McMahon, J. R., Vose, R. S., and Yin, X.: Changes in weather and climate extremes: State of knowledge relevant to air and water quality in the United States. <i>Journal of the Air and Waste Management Association</i> , 64(2), 184–197. https://doi.org/10.1080/10962247.2013.851044 , 2014.	Formatted: Line spacing: single
1954		
1955		
1956		Deleted: et al., ...ose, R. S., and Yin, X. (2014)... Changes in weather and climate extremes: State of knowledge relevant to air and water quality in the United States. <i>Journal of the Air and Waste Management Association</i> , 64(2), 184–197. ... [106]
1957		
1958	Powell, D. C., and Elderkin, C. E.: An investigation of the application of Taylor's hypothesis to atmospheric boundary layer turbulence. <i>Journal of the Atmospheric Sciences</i> , 31, 990–1002. <a href="https://doi.org/10.1175/1520-0469(1974)031<0990:AIOTAO>2.0.CO;2">https://doi.org/10.1175/1520-0469(1974)031<0990:AIOTAO>2.0.CO;2 , 1974.	Formatted ... [107]
1959		
1960		
1961		
1962	Powell, M. D., Vickery, P. J., and Reinhold, T. A.: Reduced drag coefficient for high wind speeds in tropical cyclones. <i>Nature</i> , 422(6929), 279–283. https://doi.org/10.1038/nature01481 , 2003.	Formatted: Hyperlink, Font: (Default) DengXian, (Asian) DengXian, 10.5 pt, Complex Script Font: 11 pt
1963		
1964		Deleted: &...nd Reinhold, T. A. (2003)... Reduc... [108]
1965	Prein, A. F., Coen, J., and Jaye, A.: The character and changing frequency of extreme California fire weather. <i>Journal of Geophysical Research: Atmospheres</i> , 127, e2021JD035350. https://doi.org/10.1029/2021JD035350 , 2022.	Formatted ... [109]
1966		
1967		Deleted: ¶ ... [110]
1968	Pryor, S. C., and Barthelmie, R. J.: Climate change impacts on wind energy: A review. <i>Renewable and Sustainable Energy Reviews</i> , 14(1), 430–437. https://doi.org/10.1016/j.rser.2009.07.028 , 2010.	Formatted: Hyperlink, Font: (Default) DengXian, (Asian) DengXian, 10.5 pt, Complex Script Font: 11 pt
1969		
1970		Deleted: &...nd Barthelmie, R. J. (2010)... Climat... [111]
		Formatted ... [112]

2059 Pryor, S. C., and Barthelmie, R. J.: Assessing climate change impacts on the near-term
 2060 stability of the wind energy resource over the USA. *Climate Dynamics*, 108,
 2061 8167–8171. <https://doi.org/10.1007/s00382-010-0955-3>, 2011.

2062 Pryor, S. C., Barthelmie, R. J., and Schoof, J. T.: Past and future wind climates over the
 2063 contiguous USA based on the North American Regional Climate Change
 2064 Assessment Program model suite. *Journal of Geophysical Research*, 117(D19),
 2065 D19119. <https://doi.org/10.1029/2012JD017449>, 2012.

2066 Pryor, S. C., and Barthelmie, R. J.: A global assessment of extreme wind speeds for
 2067 wind energy applications. *Nature Energy*, 6(3), 268–276,
 2068 <https://doi.org/10.1038/s41560-020-00773-7>, 2021.

2069 Raupach, M.R.: Simplified expressions for vegetation roughness length and zero-plane
 2070 displacement as functions of canopy height and area index. *Boundary-Layer
 2071 Meteorol.*, 71, 211–216. <https://doi.org/10.1007/BF00709229>, 1994.

2072 Rocque, M. N., and Rasmussen, K. L.: The Impact of Topography on the Environment
 2073 and Life Cycle of Weakly and Strongly Forced MCSs during RELAMPAGO.
 2074 *Mon. Wea. Rev.*, 150, 2317 – 2338. <https://doi.org/10.1175/MWR-D-22-0049.1>,
 2075 2022.

2076 Romanic, D., Chowdhury, J., Chowdhury, J., and Hangan, H.: Investigation of the
 2077 transient nature of thunderstorm winds from Europe, the united states, and
 2078 Australia using a new method for detection of changepoints in wind speed records.
 2079 *Mon. Wea. Rev.*, 148(9), 3747–3771. <https://doi.org/10.1175/MWR-D-19-0312.1>,
 2080 2020.

2081 Shao, X., Zhang, N., Peng, Z., Zhao, K., Luo, Y., and Song, X.: Observed surface drag
 2082 coefficient under high wind speed conditions and the relationship with coherent
 2083 structures. *Journal of Geophysical Research: Atmospheres*, 127(3),
 2084 <https://doi.org/10.1029/2021jd035301>, 2022.

2085 Shao, X., Zhang, N., and Tang, J.: A physical model for the observed inverse energy
 2086 cascade in typhoon boundary layers. *Geophysical Research Letters*, 50(18),
 2087 <https://doi.org/10.1029/2023gl105546>, 2023a.

2088 Shao, X., Zhang, N., and Tang, J.: The impact of observed drag reduction over land on
 2089 typhoon forecasting. *Journal of Geophysical Research: Atmospheres*, 128(17),
 2090 <https://doi.org/10.1029/2022jd038278>, 2023b.

2091 Shapiro, A., Potvin, C. K., and Jidong, G.: Use of a vertical vorticity equation in
 2092 variational dual-Doppler wind analysis. *J. Atmos. Oceanic Technol.*, 26, 2089 –
 2093 2106, 2009.

2094 Shi, Y., and Hu, F.: Ramp-like PM_{2.5} accumulation process and Z-less similarity in the
 2095 stable boundary layer. *Geophysical Research Letters*, 47(3), e2019GL086530,
 2096 <https://doi.org/10.1029/2019gl086530>, 2020.

2097 Shi, Y., Hu, F., Xiao, Z. S., Fan, G. Q., and Zhang, Z.: Comparison of four different
 2098 types of planetary boundary layer heights during a haze episode in Beijing.
 2099 *Science of the Total Environment*, 711, 134928,
 2100 <https://doi.org/10.1016/j.scitotenv.2019.134928>, 2020.

2101 Smith, R. B.: The influence of mountains on the atmosphere. *Advances in Geophysics*,

Deleted: &...nd Barthelmie, R. J. (2011)... Assessing climate change impacts on the near-term stability of the wind energy resource over the USA. *Climate Dynamics*, 108, 8167–8171. (... [113])

Formatted (... [114])

Deleted: Pryor, S. C., & Barthelmie, R. J. (2021). A global assessment of extreme wind speeds for wind energy applications. *Nature Energy*, 6(3), 268–276. <https://doi.org/10.1038/s41560-020-00773-7> (... [115])

Formatted (... [116])

Formatted: Line spacing: single

Formatted: Font: (Default) Times New Roman, (Asian) +Body Asian (SimSun), 12 pt, Complex Script Font: 12 pt

Formatted: Line spacing: single

Formatted (... [117])

Deleted: &...nd Hangan, H. (2020)... Investigation of the transient nature of thunderstorm winds from Europe, the united states, and Australia using a new method for detection of changepoints in wind speed records. *Mon. Wea. Rev.*, 148(9), 3747–3771. (... [118])

Formatted (... [119])

Deleted: ¶

Deleted: &...nd Song, X. (2022)... Observed surface drag coefficient under high wind speed conditions and the relationship with coherent structures. *Journal of Geophysical Research: Atmospheres*, 127(3). (... [120])

Formatted (... [121])

Deleted: &...nd Tang, J. (2023a). ... A physical model for the observed inverse energy cascade in typhoon boundary layers. *Geophysical Research Letters*, 50(18). (... [122])

Formatted (... [123])

Deleted: &...nd Tang, J. (2023b)... The impact of observed drag reduction over land on typhoon forecasting. *Journal of Geophysical Research: Atmospheres*, 128(17). (... [124])

Formatted (... [125])

Deleted: &...nd Jidong, G. (2009). (... [126])

Deleted: &...nd Hu, F. (2020). (... [127])

Formatted: Subscript

Deleted: .

Formatted (... [128])

Deleted: &...nd Zhang, Z. (2020)... Comparison of four different types of planetary boundary layer heights during a haze episode in Beijing. *Science of the Total Environment*, 711, 134928. (... [129])

Formatted (... [130])

2182 Academic Press, 21: 87-230, [https://doi.org/10.1016/S0065-2687\(08\)60262-9](https://doi.org/10.1016/S0065-2687(08)60262-9),
2183 1979.

2184 Su, T. N., Li, Z. Q., and Zheng, Y. T.: Cloud-Surface Coupling Alters the Morning
2185 Transition from Stable to Unstable Boundary Layer. *Geophys. Res. Lett.*, 50,
2186 e2022GL102256, <https://doi.org/10.1029/2022gl102256>, 2023.

2187 Tang, J., Byrne, D., Zhang, J. A., Wang, Y., Lei, X.-T., Wu, D., Fang, P., and Zhao, B.:
2188 Horizontal transition of turbulent cascade in the near-surface layer of tropical
2189 cyclones. *Journal of the Atmospheric Sciences*, 72(12), 4915 - 4925,
2190 <https://doi.org/10.1175/jas-d-14-0373.1>, 2015.

2191 Taszarek, M., Pilgaj, N., Orlikowski, J., Surowiecki, A., Walczakiewicz, S., Pilorz, W.,
2192 et al.: Derecho evolving from a mesocyclone—A study of 11 August 2017 severe
2193 weather outbreak in Poland: Event analysis and high-resolution simulation.
2194 *Monthly Weather Review*, 147, 2283–2306, <https://doi.org/10.1175/MWR-D-18-0330.1>, 2019.

2196 Taylor, G. I.: The spectrum of turbulence. *Proc. R. Soc. London*, A164, 476-490, 1938.

2197 Torralba, V., Doblaz-Reyes, F. J., and Gonzalez-Reviriego, N.: Uncertainty in recent
2198 near-surface wind speed trends: A global reanalysis intercomparison.
2199 *Environmental Research Letters*, 12(11), 114019, <https://doi.org/10.1088/1748-9326/aa8a58>, 2017.

2201 Tucker, S. C., Senff, C. J., Weickmann, A. M., Brewer, W.A., Banta, R. M., Sandberg,
2202 S. P., Law, D.C., and Hardesty, R.M.: Doppler lidar estimation of mixing height
2203 using turbulence, shear, and aerosol profiles. *J. Atmos. Ocea. Tech.* 26(4), 673 -
2204 688, <https://doi.org/10.1175/2008JTECHA1157.1>, 2009.

2205 Vose, R. S., Applequist, S., Bourassa, M. A., Pryor, S. C., Barthelmie, R. J., Blanton,
2206 B., et al.: Monitoring and understanding changes in extremes: Extratropical storms,
2207 winds, and waves. *Bulletin of the American Meteorological Society*, 95(3), 377–
2208 386, <https://doi.org/10.1175/BAMS-D-12-00162.1>, 2014.

2209 Wakimoto, R. M., Murphey, H. V., Davis, C. A., and Atkins, N. T.: High winds
2210 generated by bow echoes. Part II: The relationship between the mesovortices and
2211 damaging straight-line winds. *Mon. Wea. Rev.*, 134, 2813 - 2829,
2212 <https://doi.org/10.1175/MWR3216.1>, 2006.

2213 Wandishin, M. S., Stensrud, D. J., Mullen, S. L., and Wicker, L. J.: On the predictability
2214 of mesoscale convective systems: Three-dimensional simulations. *Monthly
2215 Weather Review*, 138(3), 863–885, <https://doi.org/10.1175/2009MWR2961.1>,
2216 2010.

2217 Weisman, M. L.: The role of convectively generated rear-inflow jets in the evolution
2218 of long-lived mesoconvective systems. *J. Atmos. Sci.*, 49, 1826–1847,
2219 [https://doi.org/10.1175/1520-0469\(1992\)049<1826:TROCGR>2.0.CO;2](https://doi.org/10.1175/1520-0469(1992)049<1826:TROCGR>2.0.CO;2), 1992.

2220 Weisman, M. L., and Davis, C. A.: Mechanisms for the generation of mesoscale
2221 vortices within quasi-linear convective systems. *J. Atmos. Sci.*, 55, 2603 - 2622,
2222 [https://doi.org/10.1175/1520-0469\(1998\)055<2603:MFTGOM>2.0.CO;2](https://doi.org/10.1175/1520-0469(1998)055<2603:MFTGOM>2.0.CO;2), 1998.

2223 Weisman, M. L., and Trapp, R. J.: Low-level mesovortices within squall lines and bow
2224 echoes. Part I: Overview and dependence on environmental shear. *Mon. Wea. Rev.*,
2225 131, 2779 - 2803, [https://doi.org/10.1175/1520-0469\(2003\)131<2779:LLMVES>2.0.CO;2](https://doi.org/10.1175/1520-0469(2003)131<2779:LLMVES>2.0.CO;2), 2003.

Deleted: , 1979

Deleted: &...nd Zheng, Y. T. (2023)... Cloud-Surface Coupling Alters the Morning Transition from Stable to Unstable Boundary Layer. *Geophys. Res. Lett.*, 50, e2022GL102256. (... [131])

Formatted: Italian

Formatted: Hyperlink, Font: (Default) DengXian, (Asian) DengXian, 10.5 pt, Complex Script Font: 11 pt

Deleted: et ... al. (2015). ...orizontal transition of turbulent cascade in the near-surface layer of tropical cyclones. *Journal of the Atmospheric Sciences*, 72(12), 4915 (... [132])

Formatted: Hyperlink, Font: (Default) DengXian, (Asian) DengXian, 10.5 pt, Complex Script Font: 11 pt

Deleted: , (2019)... Derecho evolving from a mesocyclone—A study of 11 August 2017 severe weather outbreak in Poland: Event analysis and high-resolution simulation. *Monthly Weather Review*, 147(6)... 2283–2306. ... <https://doi.org/10.1175/MWR-D-18-0330.1> (... [133])

Formatted: (... [134])

Deleted: &...nd Gonzalez-Reviriego, N. (2017)... Uncertainty in recent near-surface wind speed trends: A global reanalysis intercomparison. *Environmental Research Letters*, 12(11), 114019. (... [135])

Formatted: Spanish

Formatted: (... [136])

Deleted: &...nd Hardesty, R.M. (2009)... Doppler (... [137])

Deleted: ¶ (... [138])

Field Code Changed

Formatted: German

Deleted: ¶ (... [139])

Field Code Changed

Deleted: &...nd Wicker, L. J. (2010)... On the (... [140])

Formatted: (... [141])

Deleted: (1992)... The role of convectively gener (... [142])

Formatted: (... [143])

Deleted: &...nd Davis, C. A. (1998)... Mechanism (... [144])

Formatted: (... [145])

Deleted: &...nd Trapp, R. J. (2003)... Low-level (... [146])

Formatted: Hyperlink, Font: (Default) DengXian, (Asian) DengXian, 10.5 pt, Complex Script Font: 11 pt

2342 [0493\(2003\)131<2779:LMWSLA>2.0.CO;2](https://doi.org/10.1175/2010WAF2222417.1), 2003.

2343 Wilson, J. W., Feng, Y., Chen, M., and Roberts, R. D.: Nowcasting challenges during
 2344 the Beijing Olympics: Successes, failures, and implications for future nowcasting
 2345 systems, *Weather Forecast.*, 25, 1691 – 1714,
 2346 <https://doi.org/10.1175/2010WAF2222417.1>, 2010.

2347 Wheatley, D. M., and Trapp, R. J.: The effect of mesoscale heterogeneity on the
 2348 Genesis and structure of mesovortices within quasi-linear convective systems.
 2349 *Monthly Weather Review*, 136(11), 4220-4241,
 2350 <https://doi.org/10.1175/2008MWR2294.1>, 2008.

2351 Wu, L., Su, H., Zeng, X., Posselt, D. J., Wong, S., Chen, S., and Stoffelen, A.:
 2352 Uncertainty of Atmospheric Winds in Three Widely Used Global Reanalysis
 2353 Datasets. *J. Appl. Meteor. Climatol.*, 63, 165 –
 2354 180, <https://doi.org/10.1175/JAMC-D-22-0198.1>, 2024.

2355 Xiao, X, Sun, J., Chen, M. X., Qie, X., Wang, Y., and Ying, Z. M.: The characteristics
 2356 of weakly forced mountain-to-plain precipitation systems based on radar
 2357 observations and high-resolution reanalysis, *J. Geophys. Res.-Atmos.*, 122,
 2358 3193 – 3213, 2017.

2359 Xiao, X, Sun, J., Chen, M. X., Qie, X., Ying, Z. M., Wang, Y., and Ji, L.: Comparison
 2360 of environmental and mesoscale characteristics of two types of mountain-to-plain
 2361 precipitation systems in the Beijing region, China, *J. Geophys. Res.-Atmos.*, 124,
 2362 6856 – 6872, 2019.

2363 Xu, X., Xue, M., and Wang, Y.: The genesis of mesovortices within a real-data
 2364 simulation of a bow echo system. *J. Atmos. Sci.*, 72, 1963 – 1986.
 2365 <https://doi.org/10.1175/JAS-D-14-0209.1>, 2015a.

2366 Xu, X., Xue, M., and Wang, Y.: Mesovortices within the 8 May 2009 bow echo over
 2367 the central United States: Analyses of the characteristics and evolution based on
 2368 Doppler radar observations and a high-resolution model simulation. *Mon. Wea.*
 2369 *Rev.*, 143, 2266 – 2290, <https://doi.org/10.1175/MWR-D-14-00234.1>, 2015b.

2370 Xu, X., Ju, Y., Liu, Q., Zhao, K., Xue, M., Zhang, S., Zhou, A., Wang, Y., and Tang,
 2371 Y.: Dynamics of Two Episodes of High Winds Produced by an Unusually Long-
 2372 Lived Quasi-Linear Convective System in South China. *J. Atmos. Sci.*, 81, 1449 –
 2373 1473, <https://doi.org/10.1175/JAS-D-23-0047.1>, 2024.

2374 Yanai, M., and Nitta, T.: Computation of vertical motion and vorticity budget in a
 2375 Caribbean easterly wave, *J. Meteor. Soc. Japan*, 45, 444 – 466, 1967.

2376 Yang, H., and Du, Y.: Distinct Convection Initiation Near and Far ahead of an Idealized
 2377 Squall Line. *J. Atmos. Sci.*, 83, 151–168, [https://doi.org/10.1175/JAS-D-25-0073.](https://doi.org/10.1175/JAS-D-25-0073.2026)
 2378 2026.

2379 Zhang, D.-L., and Gao, K.: Numerical simulation of an intense squall line during 10 –
 2380 11 June 1985 PRE-STORM. Part II: Rear inflow, surface pressure perturbations
 2381 and stratiform precipitation. *Monthly Weather Review*, 117(9), 2067 – 2094, 1989.

2382 Zhang, L., Sun, J., Ying, Z., and Xiao, X.: Initiation and development of a squall line
 2383 crossing Hangzhou Bay. *Journal of Geophysical Research: Atmospheres*, 126(1),
 2384 <https://doi.org/10.1029/2020JD032504>, 2021.

2385 Zhou, A., Zhao, K., Lee, W.-C., Huang, H., Hu, D., and Fu, P.: VDRAS and

Deleted: &...nd Roberts, R. D. (2010)... Nowcasting challenges during the Beijing Olympics: Successes, failures, and implications for future nowcasting systems, *Weather Forecast.*, 25, 1691 – 1714. (... [147])

Formatted: Hyperlink, Font: (Default) DengXian, (Asian) DengXian, 10.5 pt, Complex Script Font: 11 pt

Deleted: &...nd Trapp, R. J. (2008)... The effect of mesoscale heterogeneity on the Genesis and structure of mesovortices within quasi-linear convective systems. *Monthly Weather Review*, 136(11), 4220-4241. (... [148])

Deleted: :

Formatted: (... [149])

Formatted: Font: Times New Roman, 12 pt, Complex Script Font: 12 pt

Deleted: Su, Zeng (... [150])

Deleted: Posselt... Wong, S. Wong... Chen, S. Chen... and Stoffelen, A. Stoffelen, (2024)... Uncertainty of Atmospheric Winds in Three Widely Used Global Reanalysis Datasets. *J. Appl. Meteor. Climatol.*, 63 (... [151])

Formatted: German

Formatted: (... [152])

Deleted: &...nd Ying, Z. M. (2017). (... [153])

Deleted: &...nd Ji, L. (2019). (... [154])

Deleted: &...nd Wang, Y. (2015a). (... [155])

Formatted: Hyperlink, Font: (Default) DengXian, (Asian) DengXian, 10.5 pt, Complex Script Font: 11 pt

Deleted: &...nd Wang, Y. (2015b)... Mesovortices within the 8 May 2009 bow echo over the central United States: Analyses of the characteristics and evolution based on Doppler radar observations and a high-resolution model simulation. *Mon. Wea. Rev.*, 143, 2266 – 2290. (... [156])

Formatted: (... [157])

Deleted: Xu, X., and Coauthors (2024)... Dynamic (... [158])

Formatted: (... [159])

Deleted: &...nd Nitta, T. (1967). (... [160])

Formatted: Finnish

Formatted: Line spacing: single

Deleted: &...nd Gao, K. (1989). (... [161])

Deleted: &...nd Xiao, X. (2021)... Initiation and (... [162])

Formatted: (... [163])

Deleted: &...nd Fu, P. (2020). (... [164])

2466 polarimetric radar investigation of a bow echo formation after a squall line merged
2467 with a preline convective cell. J. Geophys. Res. Atmos., 125, e2019JD031719.
2468 <https://doi.org/10.1029/2019JD031719>, 2020.
2469 Zhou, X., Zhang, C., Xiao, Z., Li, Y., and Lu, G.: Inverse Energy Cascades in the
2470 Boundary Layer During Strong Winds Based on Doppler Lidar. Geophysical
2471 Research Letters, 52(2), <https://doi.org/10.1029/2024GL113273>, 2025.
2472

Formatted: Hyperlink, Font: (Default) DengXian, (Asian)
DengXian, 10.5 pt, Complex Script Font: 11 pt

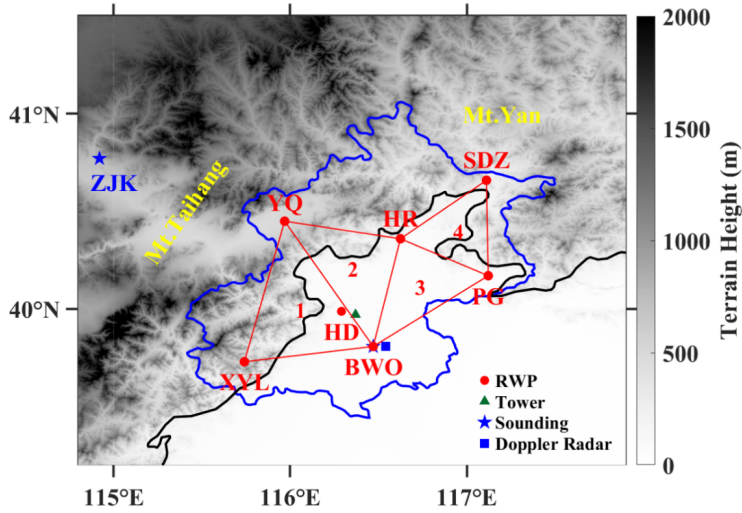
Deleted: &

Deleted: (2025).

Deleted:).

2476

Figures



2477

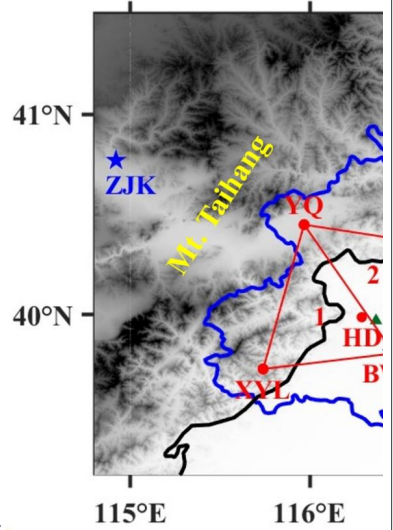
2478 **Figure 1.** Spatial distribution of the terrain height over Beijing and surrounding areas
 2479 with the black and blue line denoting the plain line at 200 m terrain elevation and the
 2480 provincial boundary, respectively. Seven RWPs (red dots) deployed at Xiayunling
 2481 (XYL; 39.73°N, 115.74°E), Shangdianzi (SDZ; 40.66°N, 117.11°E), Huairou (HR;
 2482 40.36°N, 116.63°E), Yanqing (YQ; 40.45°N, 115.97°E), Haidian (HD; 39.98°N,
 2483 116.28°E), Pinggu (PG; 40.17°N, 117.12°E), and the Beijing Weather Observatory
 2484 (BWO; 39.79°N, 116.47°E). Four red triangles with number denote the regions used to
 2485 calculate the dynamic parameters with the triangle method. Blue five-pointed stars
 2486 denote the L-band sounding at BWO and Zhangjiakou (ZJK; 40.77° N, 114.92° E)
 2487 station. A S-band Doppler weather radar (blue square) is also deployed at BWO. Green
 2488 small triangle represents the location of meteorological tower (39.97°N, 116.37°E).

2489

2490

Deleted: ¶

Deleted: ¶



Deleted: .

Formatted: Font: (Default) Times New Roman, Complex Script Font: Times New Roman

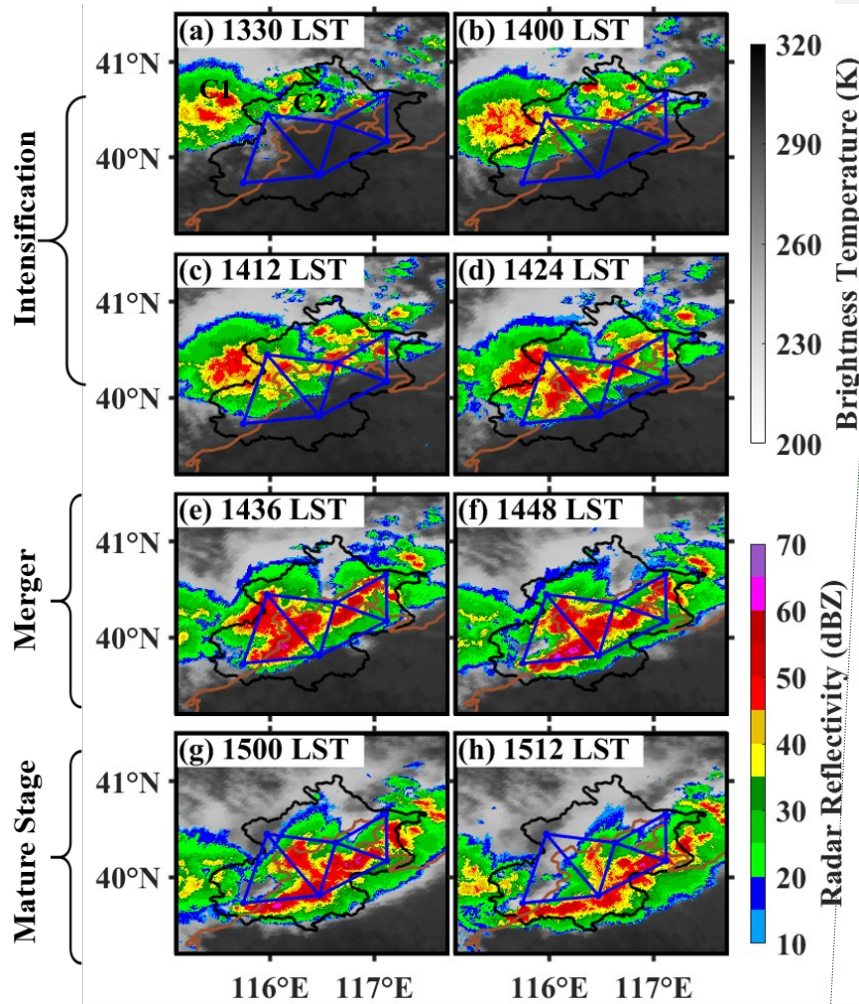
Formatted: Font: (Default) Times New Roman, Complex Script Font: Times New Roman

Deleted: boundaries

Deleted: ¶

Formatted: Font: (Asian) SimSun

Deleted: ¶

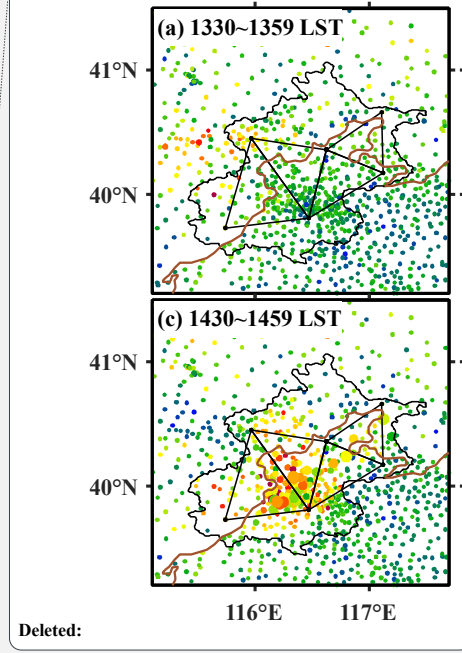
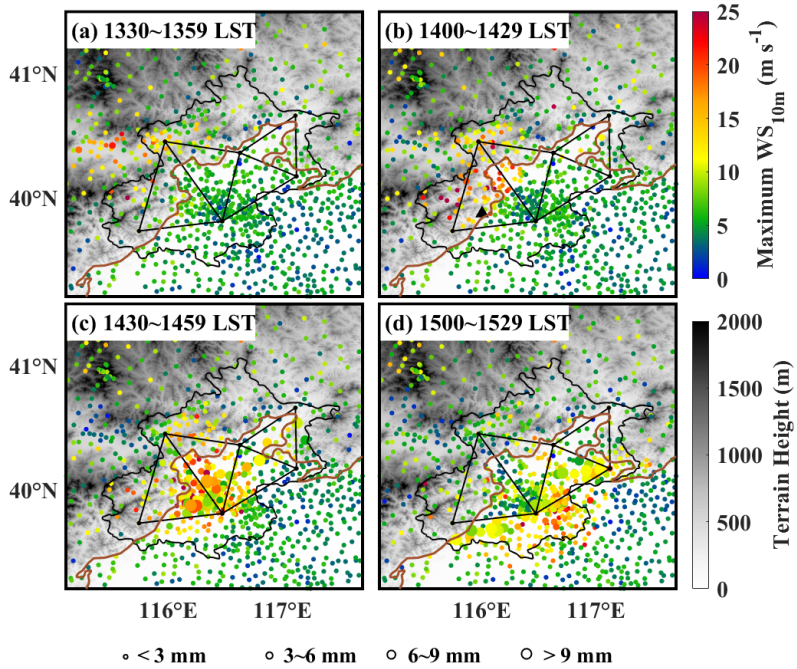


Moved (insertion) [2]

Deleted: 4

2497
2498
2499
2500
2501
2502
2503

Figure 2. Brightness temperature from 10.8 μm channel of Himawari-8 geostationary satellite (gray shadings; K), superimposed with composite radar reflectivity (color-shaded; dBZ) at (a) 1330, (b) 1400, (c) 1412, (d) 1424, (e) 1436, (f) 1448, (g) 1500, and (h) 1512 LST on 30 May 2024. The four blue triangles and brown line denote the RWP mesonet and the 200 m terrain elevation line, respectively.



Deleted:

Deleted: 2

Deleted: M

Deleted: °

Deleted: °

Formatted: Font: Times New Roman, Not Italic, Complex Script Font: Not Italic

2505

2506 **Figure 3.** Terrain height (gray shadings; m) over Beijing and surrounding areas

2507 superimposed with the maximum 10 m wind speed (shading of dots, $m s^{-1}$) observed

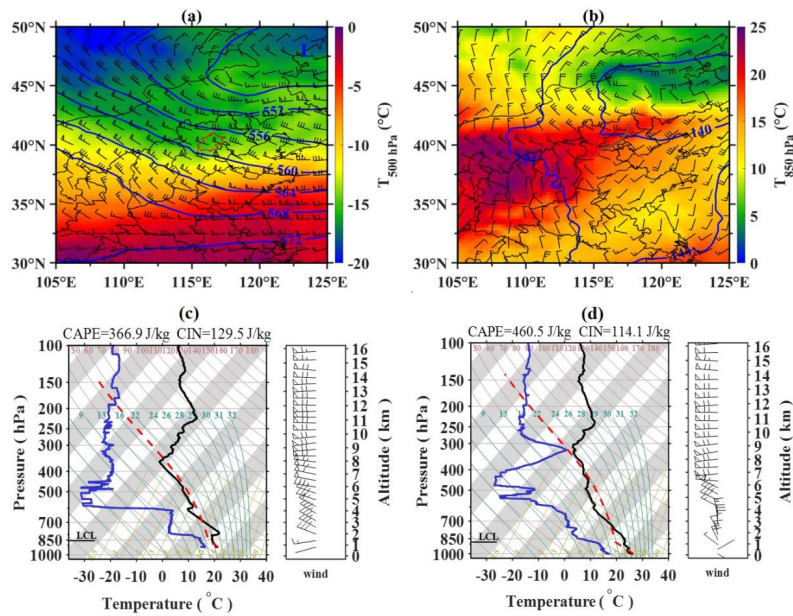
2508 during (a) 1330-1359 LST, (b) 1400-1429 LST, (c) 1430-1459 LST, and (d) 1500-1529

2509 LST. The size of dots denoted the accumulated rainfall in 30 minutes. Black small

2510 triangle in (b) represents the location of the Qianling Mountain site (39.87°N, 116.07°E).

2511

2512



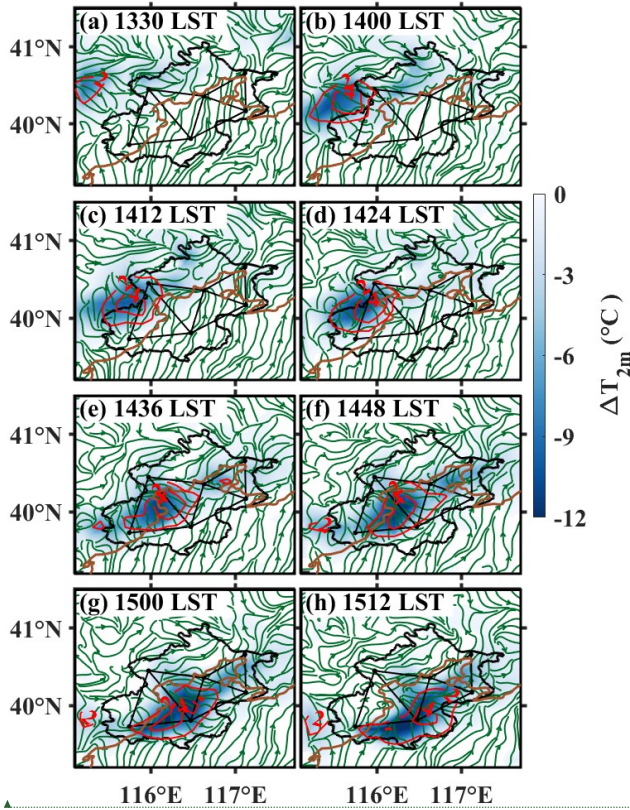
2518

2519 **Figure 4.** Horizontal distribution of temperature (color-shaded; $^{\circ}\text{C}$), geopotential
 2520 height (solid blue lines; 10 gpm) and wind barbs (a full barb is 4 m s^{-1} with a flag
 2521 denoting 20 m s^{-1}) at (a) 500 hPa and (b) 850 hPa from the ERA5 hourly reanalysis
 2522 data at 1400 LST on 30 May 2024. Note that black lines represent provincial
 2523 administrative boundaries of China. The administrative boundary of Beijing is
 2524 highlighted as red curve. The letter L denotes the center of a low-pressure system, and
 2525 the skew T-log P diagrams derived from the upper-air sounding at the ZJK (c) and
 2526 BWO (d) site at 0800 LST on 30 May 2024.

2527

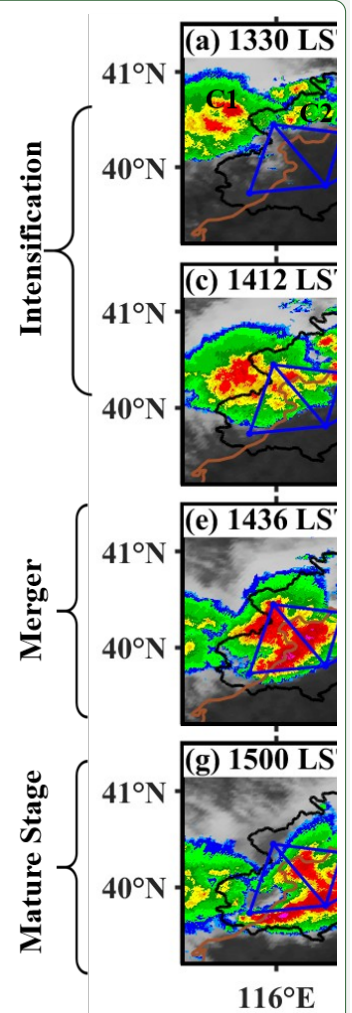
Deleted: 3

Deleted: the administrative boundary of Beijing is marked in red curve, t...



2531

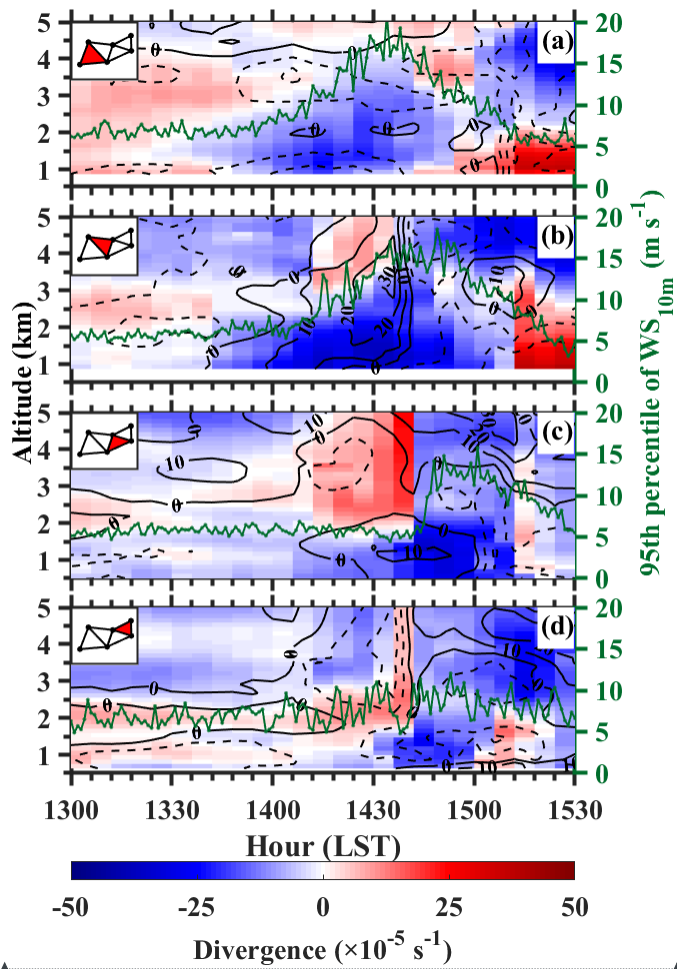
2532 **Figure 5.** Evolution of T_{2m} change (color-shaded; °C) and pressure change (solid red
 2533 lines at 2 hPa intervals) in 30 minutes, superimposed with 10 m streamlines derived
 2534 from AWSs from (a) 1300 to (h) 1512 LST on 30 May 2024.



Moved up [2]:

Figure 4. Brightness temperature from 10.8 μm channel of Himawari-8 geostationary satellite (gray shadings; K), superimposed with composite radar reflectivity (color-shaded; dBZ) at (a) 1330, (b) 1400, (c) 1412, (d) 1424, (e) 1436, (f) 1448, (g) 1500, and (h) 1512 LST on 30 May 2024. The four blue triangles and brown line denote the RWP mesonet and the 200 m terrain elevation line, respectively.¶

Page Break

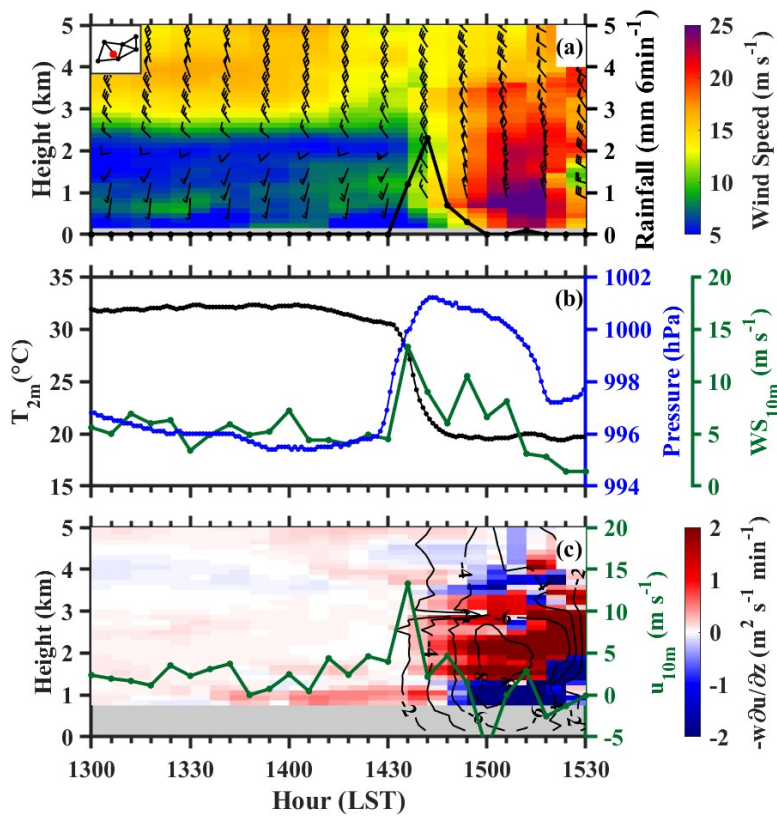


Formatted: Font: Times New Roman

Formatted: Font: Times New Roman

2544

2545 **Figure 6.** The vertical profiles of horizontal divergence (D , color shaded; s^{-1}) and
 2546 vertical vorticity (ζ , dashed/solid contours for negative/positive values; s^{-1}) in (a)
 2547 triangle 1, (b) triangle 2, (c) triangle 3, (d) triangle 4 derived from the RWP mesonet
 2548 (see their locations as the red patches on the small maps in the upper left corners) from
 2549 1300 to 1530 LST on 30 May 2024. Green dotted lines show the 95th percentile of 10
 2550 m wind speed for all stations in the triangle area at 1-min intervals.
 2551



Formatted: Font: Times New Roman

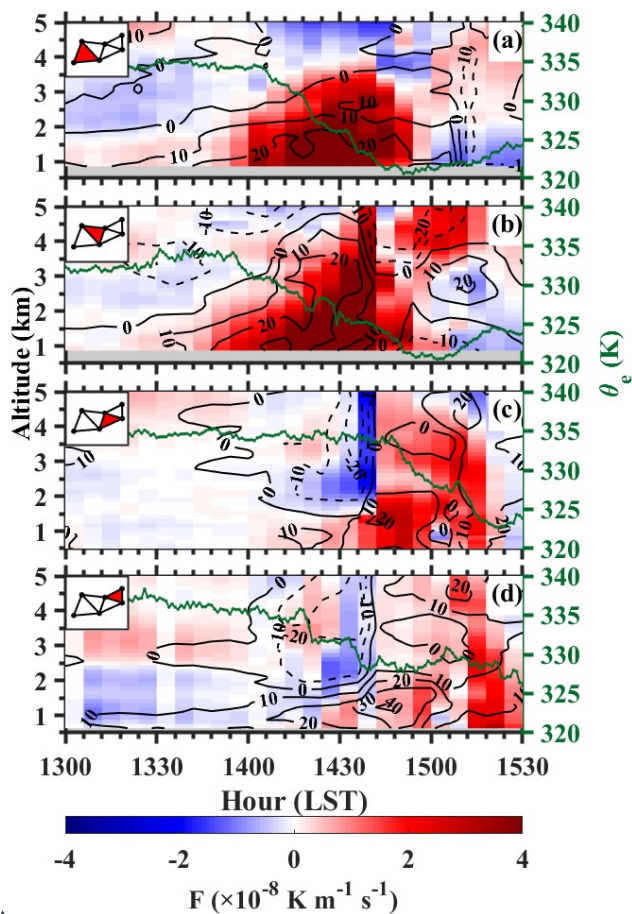
Formatted: Font: Times New Roman

2552

2553 **Figure 7.** (a) Vertical profiles of horizontal wind barbs between 0 and 5 km height,
 2554 superimposed with horizontal wind speed (shadings; m s⁻¹) at HD (see its location as
 2555 red dots on the small maps in the upper-left corners) during the period of 1300-1530
 2556 LST on 30 May 2024. The black solid line shows 6-min accumulated precipitation (mm
 2557 6min⁻¹). (b) Time series of 2m temperature (°C) in black, instantaneous 10 m wind
 2558 speed (m s⁻¹) in green, and pressure (hPa) in blue at HD; (c) Vertical advection of u
 2559 component of horizontal wind, $-w\partial u/\partial z$ (shading, m² s⁻¹ min⁻¹) superimposed with
 2560 vertical velocity (contours, m s⁻¹) at HD. The green solid line shows u component of
 2561 instantaneous 10 m wind (m s⁻¹).

2562

Formatted: Font: Times New Roman

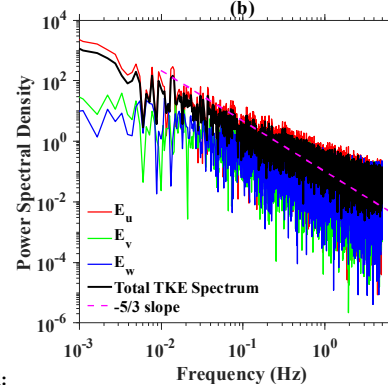
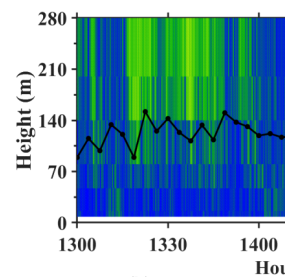


2564
 2565 **Figure 8.** Same as Figure 6, except for frontogenesis function (F , color shaded; K m^{-1}
 2566 s^{-1}) and shearing deformation (S ; contours, s^{-1}). Green dotted lines show the area-
 2567 averaged equivalent potential temperature θ_e (K) for all stations in the triangle area at
 2568 5-min intervals.
 2569

Formatted: Font: Times New Roman

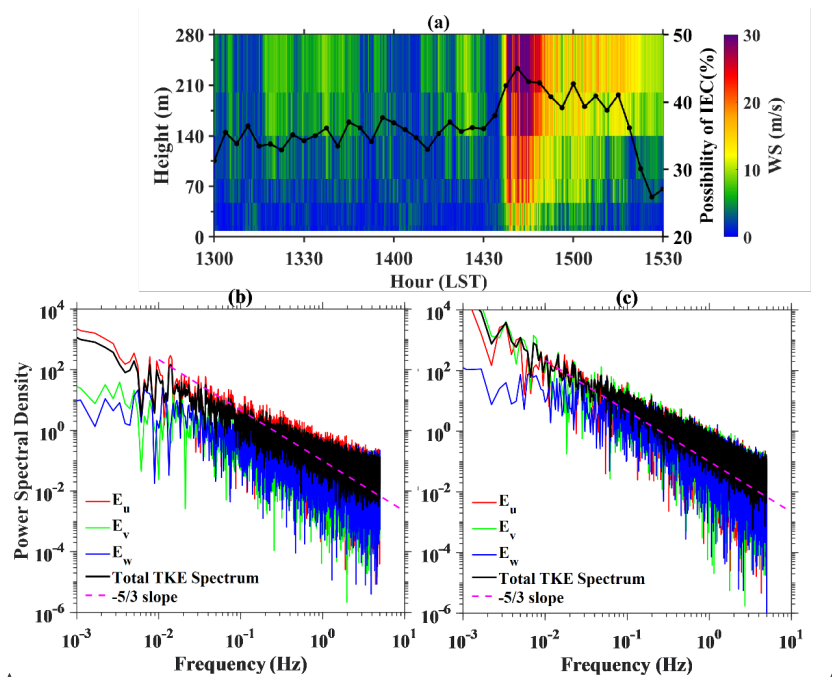
Formatted: Font: Times New Roman

Deleted: 7



Deleted:

Formatted: Font: Times New Roman

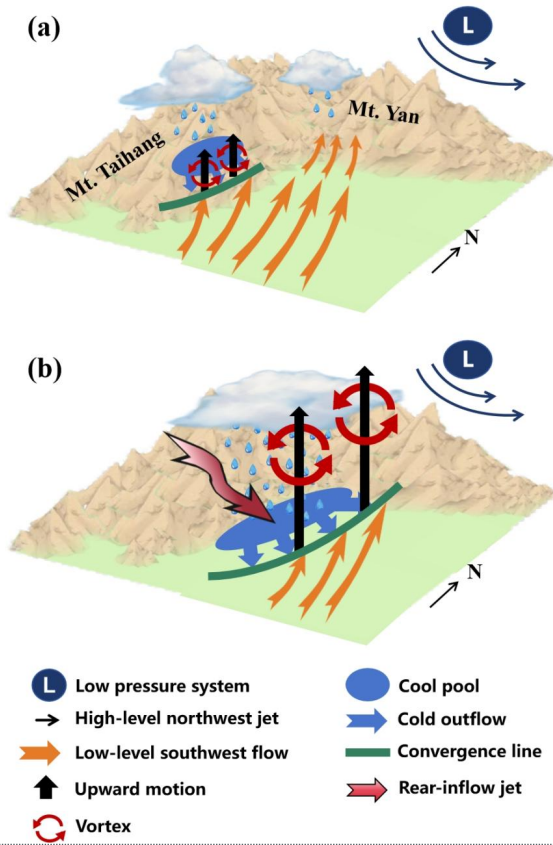


Formatted: Font: Times New Roman

Formatted: Font: Times New Roman

2572
2573
2574
2575
2576
2577
2578
2579
2580
2581
2582
2583

Figure 9. (a) Vertical profiles of horizontal wind speed (shadings; m s^{-1}) at the height of 8, 15, 47, 80, 140, 200 and 280 m during the period of 1300-1530 LST on 30 May 2024, which is directly measured from the meteorological tower (see its location in Figure 1) built and operated by the Institute of Atmospheric Physics, Chinese Academy Sciences. The black solid line shows the possibility of inverse energy cascades (IEC) at all heights. Energy spectra at the height of 280 m for components in different directions (u, v, w) during (b) 1406-1436 LST and (c) 1436-1506 LST, respectively. Dashed magenta line represents the theoretical Kolmogorov's inertial range slope $-5/3$ in frequency domain.



2584
2585
2586
2587
2588
2589

Figure 10. Conceptual model for the generation and evolution of near-surface high winds (a) before and (b) after merger of the quasi-linear convective system (QLCS) for the extreme wind event in Beijing occurring May 30, 2024.